REVISION 5

1 Revision 5

2

Mineral compositions and thermobarometry of basalts and boninites recovered during IODP Expedition 352 to the Bonin forearc

6
7

8 SCOTT A. WHATTAM[1*], JOHN W. SHERVAIS[2], MARK K. REAGAN[3], DANIEL A.

9 COULTHARD JR.[3,4], JULIAN A. PEARCE[5], PETER JONES[6], JIEUN SEO[7], KEITH

10 PUTIRKA[8], TIMOTHY CHAPMAN[9,10], DANIEL HEATON[11], HONGYAN LI[12], WENDY R.

11 NELSON[13], KENJI SHIMIZU[14] AND ROBERT J. STERN[15]

12
13 [1]Department of Geosciences, King Fahd University of Petroleum and Minerals, Dhahran 31261, Saudi Arabia
14 [2]Department of Geology, Utah State University, Logan, UT 84322-4505, USA
15 [3]Department of Earth and Environmental Sciences, University of Iowa, Iowa City, IA 52242, USA
16 [4]Volcanic Risk Solutions, Massey University, Palmerston North 4414, New Zealand
17 [5]School of Earth, Ocean and Planetary Sciences, Cardiff University, Cardiff CF10 3YE, UK
18 [6]Department of Earth Sciences, Carleton University, Ottawa, ON, K1S 5B6, Canada
19 [7]Department of Earth and Environmental sciences, Korea University, Seoul 02841, South Korea
20 [8]Department of Earth and Environmental Sciences, California State University, Fresno, CA 93740, USA
21 [9]School of Geosciences, University of Sydney, NSW 2006, Australia
22 [10]Earth Science, School of Environmental and Rural Science, University of New England, NSW 2351, Australia
23 [11]College of Earth, Ocean and Atmospheric Sciences, Oregon State University, Corvalis, OR 97331-5503, USA
24 [12]State Key Laboratory of Isotope Geochemistry, Guangzhou Institute of Geochemistry, Chinese Academy of
25 Sciences, Guangzhou 510640, PR China
26 [13]Department of Physics, Astronomy and Geosciences, Towson University, Towson, MD 21252, USA
27 [14]Kochi Institute for Core Sample Research, Japan Agency for Marine-Earth Science and Technology, Monobe-otsu
28 200, Nankoku, Kochi, 783-8502, Japan
29 [15]Geosciences Department, University of Texas at Dallas, Richardson, TX 75083-0688, USA

30
31 Words: 7330 excluding abstract

32
33
34
35 * Corresponding author. Tel.: 966 55 646 6238
36 E-mail address: sawhatta@gmail.com
37

REVISION 5

38   **ABSTRACT**

39   Central aims of IODP Expedition 352 were to delineate and characterize the magmatic

40   stratigraphy in the Bonin forearc in order to define key magmatic processes associated with

41   subduction initiation and their potential links to ophiolites. Expedition 352 penetrated 1.2 km of

42   magmatic basement at four sites and recovered three principal lithologies: tholeiitic forearc

43   basalt (FAB), high-Mg andesite and boninite, with subordinate andesite. Boninites are

44   subdivided into basaltic, low-Si and high-Si varieties. The purpose of this study is to determine

45   conditions of crystal growth and differentiation for Expedition 352 lavas and compare and

46   contrast these conditions with those recorded in lavas from mid-ocean ridges, forearcs and

47   ophiolites. Results show that Cr# (cationic Cr/Cr+Al) vs. TiO_2 relations in spinel and

48   clinopyroxene demonstrate a trend of source depletion with time for the Expedition 352 forearc

49   basalt to boninite sequence that is similar to sequences in the Oman and other suprasubduction

50   zone ophiolites. Clinopyroxene thermobarometry results indicate that FAB crystallized at

51   temperatures (1142-1190°C) within the range of MORB (1133-1240°C). When taking into

52   consideration liquid lines of descent of boninite, orthopyroxene barometry and olivine

53   thermometry of Expedition 352 boninites demonstrate that they crystallized at temperatures

54   marginally lower than those of FAB, between ~1119°C and ~1202°C and at relatively lower

55   pressure (~0.2-0.4 kbar vs. 0.5-4.6 kbar for FAB). Elevated temperatures of boninite

56   orthopyroxene (~1214°C for low-Si boninite and 1231-1264°C for high-Si boninite) may suggest

57   latent heat produced by the rapid crystallization of orthopyroxene. The lower pressure of

58   crystallization of the boninite may be explained by their lower density and hence higher ascent

59   rate, and shorter distance of travel from place of magma formation to site of crystallization,

60   which allowed the more buoyant and faster ascending boninites to rise to shallower levels before

61   crystallizing, thus preserving their high temperatures.

62   **Keywords:** International Ocean Discovery Program (IODP), JOIDES Resolution, Expedition

63   352, Izu-Bonin-Mariana Fore Arc, forearc basalt, boninite, ophiolite, Sites U1439, U1440, U1441, U1442

64

65   **INTRODUCTION**

66   A strong genetic link between ophiolites and intra-oceanic arc systems has been

67   recognized for some time (Miyashiro 1973; Alabaster et al. 1982), and a more specific linkage

68   with subduction initiation has been made more recently (Stern and Bloomer 1992; Shervais 2001;

69   Pearce and Robinson 2010; Whattam and Stern 2011; Stern et al. 2012; Moghadam et al. 2014).

70   Nonetheless, controversy as to whether ophiolites mostly form in magmatic arcs or at mid-ocean

71   ridges has persisted because, from a chemical and structural point of view, some ophiolites have

72   chemical compositions like those of mid-ocean ridge basalt (MORB) while many others have

73   chemical compositions like those of arcs. Part of this confusion lies in the fact that many

74   ophiolites contain both a MORB-like unit and a volcanic arc-like unit, which suggests formation

75   of each suite in two distinct tectonic environments. The early identification of the MORB-like

76   component led to the interpretation that ophiolites are obducted remnants of normal oceanic

77   lithosphere, like those produced today at the Mid-Atlantic Ridge or East Pacific Rise (e.g.,

78   Coleman, 1981; Moores 1982), but further study has consistently identified an arc-like chemical

79   signature in most ophiolites (see Metcalf and Shervais 2008 for a review of the 'ophiolite

80   conundrum'). The recognition of MORB- and arc-like magmas has led to the interpretation that

81   ophiolites represent fragments of oceanic lithosphere generated in supra-subduction zone settings

82   (Miyashiro, 1973; Pearce et al. 1984; Pearce 2003; Saccani and Photiades 2004; Dilek and Shallo

83   2007; Dilek et al. 2008; Moghadam and Stern 2014) with many studies suggesting formation

84   within back arc basins (e.g., Evans et al., 1991; Monnier et al. 1995; Thompson et al. 1997;

85   Cluzel et al. 2001; Saccani et al. 2008), to reconcile the chemical bimodality. Models entailing

86   formation above a reconfigured subduction zone subsequent to a major tectonic reorganization

87   and establishment of a new subduction zone within the original mid-ocean ridge or back arc were

88   also advanced (see review of Whattam 2009).

89   A key breakthrough in reconciling these perspectives was the discovery that the most

90   abundant lavas cropping out on the Mariana (Reagan et al. 2010, 2013), Izu (DeBari et al., 1999),

91   and Bonin (Ishizuka et al. 2011) forearc trench slopes were MORB-like tholeiites termed

92   'forearc basalts' (or 'FAB'; Reagan et al., 2010). These FAB are older than boninites exposed

93   upslope in the forearc (cf. Ishizuka et al., 2006, 2011; Reagan et al., 2019), suggesting that

94   seafloor spreading occurred immediately after subduction initiation to generate FAB and that

95   boninites were generated later after fluids from the subducting slab became involved in magma

96   genesis (Reagan et al., 2017). In an effort to extend these insights from marine geology on land,

97   the subduction initiation rule of Whattam and Stern (2011) hypothesizes that all magmatic

98   components (i.e., MORB, arc basalt, and boninite) of most well-preserved ophiolites form in

99   similar proto-forearc settings and follow a predictable chemotemporal progression as a new

100   subduction zone forms. This model is consistent with the hypothesis that seafloor spreading in a

101   proto-forearc environment accompanies subduction initiation (Shervais, 2001; Stern et al., 2012).

102   The motivating force behind IODP Expedition 352, which drilled into the outer Bonin

103   forearc was to test the aforementioned models. Here, we analyze the compositions of minerals

104   from Expedition 352 lavas to determine the conditions of crystal growth and differentiation. We

105   then compare and contrast the mineral compositions and thermobarometry with those of MORB

4

106 and ophiolites, specifically testing the hypothesis that ophiolites are more closely linked to

107 subduction initiation rather than to regular ocean basin sea-floor spreading.

108

GEOLOGIC AND TECTONIC BACKGROUND

110   The IBM intra-oceanic arc stretches 2,800 km from the Izu peninsula, Japan to seamounts

111 west of Guam, USA (Figure 1). The IBM represents one of the most intensely studied intra-

112 oceanic arcs on Earth, as numerous drilling expeditions, including IODP Expedition 352,

113 manned submersible dives, and dredging cruises on and along the forearc have targeted this

114 archtypical geologic setting (e.g. Bloomer and Hawkins, 1983; Ishizuka et al. 2006, 2011;

115 Reagan et al. 2010, 2013, 2015, 2017;). Some suggest that the IBM subduction zone began due

116 to hemispheric-scale foundering of old, dense lithosphere comprising the western segment of the

117 Pacific Plate and its ultimate subduction to the west beneath the Philippine Sea Plate (Stern and

118 Bloomer, 1992; Bloomer et al. 1995; Stern et al. 2012). Leng and Gurnis (2015) however,

119 propose an alternative model entailing the combination of thermal and compositional density

120 contrasts between the overriding relic arc and adjacent old Pacific oceanic plate, the conditions

121 of which promoted spontaneous subduction initiation (see also Stern and Bloomer, 1992; Niu et

122 al. 2002). A third model postulates that subduction was nucleated above the Manus plume

123 (0°N/150°E) near the Pacific-East Asian Sea plate boundary circa in the middle Eocene

124 (Macpherson and Hall, 2001; Wu et al., 2016). Large-scale formation of seafloor crust in the

125 IBM forearc after subduction initiation began between 52.5 and 51.9 Ma (Ishizuka et al. 2011;

126 Reagan et al. 2013; Reagan et al., 2019). The Philippine Sea plate subsequently migrated

127 northward and was accompanied by post-40 Ma maximum 80° clockwise rotation. The

128   predominantly submarine convergent plate boundary is thus the result of ~52 My of subduction

129   of the Pacific Plate beneath the eastern margin of the Philippine Sea Plate.

130   The sequence of initial magmatic products preserved in the IBM forearc is "ophiolite-

131   like" and is similar everywhere the forearc has been sampled (Bloomer and Hawkins 1983; Stern

132   and Bloomer 1992; DeBari et al., 1999; Reagan et al. 2010, 2013, 2017; Ishizuka et al. 2011).

133   This commonality implies that a short (<1 Ma), but intense episode of asthenospheric upwelling,

134   magmatism, and seafloor spreading to generate FAB-related crust occurred immediately after

135   subduction initiation (Reagan et al., 2019). This zone of upwelling, melting and magmatism

136   occurred over tens to hundreds of kilometers across the entire arc (Arculus et al., 2015; Hickey-

137   Vargas et al., 2018; Yogodzinski et al., 2018). Boninite volcanism followed closely after FAB,

138   beginning at *c.* 51.3 Ma and lasting through to *c.* 46 Ma (Ishizuka et al. 2006, 2011; Reagan et

139   al., 2019).

140   The presence of boninites is in itself an important tectonic indicator. Numerous

141   petrological, geochemical, and experimental studies (e.g. Crawford 1989; Umino and Kushiro

142   1989; van der Laan et al. 1989; Pearce et al. 1992; Taylor et al. 1994; Kushiro 1972, 1974; Green

143   1973, 1976; Mitchell and Grove, 2015) have suggested that boninite magmas are generated via

144   high degrees of partial melting (of the order of >20%) of refractory mantle fluxed with slab-

145   derived fluids or melts in subduction environments with modest temperatures (~1130-1275°C)

146   and low pressure (0.3-1.7 kbar; see reviews by Kushiro, 2007; Pearce and Reagan, 2019).

147   Subsequent to boninite production in the IBM forearc, igneous activity retreated

148   westward towards where the magmatic arc is today. This later activity was characterized by the

149   production of normal arc tholeiitic and calc-alkaline magmas beginning at *c.* 45 Ma, thereby

150   marking the establishment of a mature and stable magmatic arc system (Ishizuka et al. 2006;

151   2011; Reagan et al., 2008).

152

153   **STUDY AREA**

154   IODP Expedition 352 drilled the northern IBM forearc to the immediate northeast of the

155   Bonin Islands between 142°30'E and 143°00'E and 28°24'N and 28°27'N (Reagan et al. 2015)

156   (Figure 1b). Four drill sites were cored: U1440 and U1441 are closest to the trench and U1439

157   and U1442 are upslope and to the west (Figure 1c). Sites U1440 and U1441 recovered FAB and

158   related hypabyssal rocks (dolerite dikes, Reagan et al., 2017; Shervais et al., 2019), whereas

159   boninite series and high-Mg andesite lavas were recovered from Sites U1439 and U1442. A total

160   of 1.22 km of magmatic basement was cored.

161   Expedition 352 results suggest FAB erupted shortly after subduction initiation and were

162   generated by seafloor spreading, as evidenced by the widespread presence of mafic dikes, with

163   little to no subduction input and compositions similar to those of the most depleted MORB

164   (Reagan et al., 2017; Shervais, et al., 2019). Subsequent to extraction of FAB, continued melting

165   of a more depleted mantle caused by fluxing of subduction components is inferred to result in the

166   generation of the boninites. This succession is analogous to that recorded by many ophiolites,

167   thus providing a direct link between subduction initiation, forearc spreading and ophiolite

168   genesis (Stern and Bloomer, 10092; Shervais, 2001; Reagan et al., 2010; Whattam and Stern,

169   2011; Stern et al., 2012; Reagan et al., 2017)

7

METHODS

Electron probe micro analyzer

Approximately 70 samples of tholeiitic FAB, high-Mg andesite, boninite, and subordinate andesite were chosen for electron probe micro-analyzer (EPMA) analysis. Quantitative analyses were made on an automated 4 spectrometer Cameca Camebax MBX electron probe housed in the Department of Earth Sciences, Carleton University (Ottawa, Canada) by the wavelength dispersive X-ray analysis method (WDX). Operating conditions involved a 20kv accelerating potential and a beam current of 20 nA. Beam sensitive minerals such as feldspar, were analyzed using a rastered electron beam of ~ 8 x 8 microns in size and a focused beam size of 1 micron was used for microlites of clinopyroxene and feldspar. Alkali elements such as Na and K were analyzed first. Peak counting times were *c.* 15–20 seconds unless X-ray counts exceeded 40,000. Background positions were chosen carefully to avoid interferences from adjacent peaks and measurements were made at 50% of the peak counting time. Raw X-ray data were converted to elemental weight % by the Cameca PAP matrix correction program. A suite of well characterized natural and synthetic minerals and compounds were used as primary and secondary calibration standards. Kakanui kaersutite K1 and USNM Kakanui hornblende and USNM chromium augite (Reay el al, 1989; Jarosewhich et al, 1980) were analyzed as internal standards to monitor data quality. Analyses are accurate to 1–2 % for major elements (>10 wt %) and 3–10 % relative for minor elements (0.5–10%) As the detection limit is approached (<0.1 wt %), relative errors approach 100 %. Throughout the text, we refer to informal thin section numbers of our probed samples. Supplementary Table S1 provides corresponding formal IODP sample numbers.

192   Olivine crystals, Cr-spinel inclusions, and Cr-spinel phenocrysts were analyzed for major

193   elements using a JEOL JXA-8230 Superprobe at the University of Iowa. For olivine, the beam

194   conditions were set to 20 keV and 200 nA. Each spot was analyzed for 10.5 minutes with a dwell

195   times of 40 seconds for major elements, 90 seconds for most minor elements, and 360 seconds

196   for Al. In order to check for instrumental drift as well as ensure data quality, we analyzed San

197   Carlos Olivine grains intermittently during the analysis. Cr-spinel was measured with the beam

198   set to 20 keV and 20 nA and 1.5-minute count time. The Cr-spinel standard NMNH 117075 was

199   analyzed during the analysis as a drift monitor and for data quality assurance.

200

Thermobarometry and Mineral-melt equilibria

202   The Fe/Mg partition coefficient between olivine and basaltic liquid

203    $[(Fe/Mg)_{ol}/(Fe/Mg)_{melt}]$ is well constrained experimentally as 0.30 ± 0.03 (Roeder and Emslie

204   1970) being constant for a wide range of conditions, except for pressures higher than 10 kbar

205   (Ulmer, 1989) or for Fe-rich olivine (Fo<25) (Toplis and Carroll 1995). The Fe/Mg partition

206   coefficient between orthopyroxene and basaltic liquid is also well established at 0.29 ± 0.06 (see

207   Putrika 2008). The Fe/Mg partition coefficient between clinopyroxene and basaltic liquid is less

208   well constrained than for olivine-liquid, principally because of the presence of abundant ferric

209   iron in clinopyroxene. Although a slight compositional effect may exist (Hoover and Irvine

210   1977), $(Fe/Mg)^{cpx}/(Fe/Mg)^{melt} = 0.27\pm0.03$ is consistent with experimental results (Putirka,

211   2008), and 0.27 is adopted here.

212   Estimates of temperatures and pressure of FAB crystallization are based on compositions

213   of clinopyroxene phenocrysts and microlites using the methods, models and equations of Putirka

214   et al. (1996, 2003) and Putirka (2008). Specifically, we use equations P1 and T1 of Putirka et al.

9

215   (1996); the model of Putirka et al. (2003); and equations 30 (temperature), 33 (pressure) and 34

216   (temperature) of Putirka et al. (2006). Conditions of boninite crystallization are based on

217   orthopyroxene and olivine phenocryst compositions. Pressure estimates from orthopyroxene are

218   calculated from equations 29a, 29b and 29c of Putirka (2008) and temperatures are calculated

219   from Beattie (1993) and equations 28 and 28b of Putirka (2008). Olivine temperature estimates

220   are calculated using Beattie (1993) and equations 13-15 of Putirka (2008).

221   In order to compare the composition of clinopyroxene phenocrysts and microlites from

222   Expedition 352 FAB with those from typical MORB, we collated clinopyroxene and

223   complementary whole rock compositions from the Petrological Database (PetDB,

224   http://www.earthchem.org/petdb). Details of sample selection, collation, and manipulation of

225   PetDB MORB whole-rock and clinopyroxene samples are provided in the supplementary

226   material[1]. Pressure and temperature estimates of clinopyroxene from the PetDB MORB database

227   ($n = 75$ samples shown to exhibit clinopyroxene-melt equilibrium) are calculated using the

228   thermometer of Putirka (2008, Eqn. 33) and the barometer of Neave and Putirka (2017).

229   It is important to establish whether Expedition 352 FAB clinopyroxene phenocrysts and

230   microlites and boninite orthopyroxene and olivine phenocrysts were in equilibrium with the host

231   magma when they crystallized. If mineral-melt equilibria can be established, specific mineral-

232   melt (whole-rock composition) pairs can then be used to constrain the pressure and temperature

233   of crystallization. The demonstration of disequilibrium between specific mineral-melt pairs also

234   yields information, such as the presence of xenocrysts and/or crystal cumulates.

235   To assess mineral-melt Fe-Mg exchange for clinopyroxene, orthopyroxene and olivine

236   for our new mineral compositions, we use whole-rock compositions from Reagan et al. (2015).

237   Whole rock Mg# (i.e., $Mg^{2+}/(Mg^{2+}+Fe^{2+})$) for the FAB is calculated assuming $Fe^{3+}/FeT = 0.17$

238   (whereby FeT = Fe^{2+} + Fe^{3+}), a value that approximates crystallization at the FMQ (fayalite-

239   magnetite-quartz) oxygen buffer. For the boninites, high-Mg andesites and lone anomalous

240   andesite TS 93 (formal IODP number 352-U1439C-8R-2-W 105/107-TSB-TS_93), whole rock

241   Mg# is calculated assuming Fe^{3+}/FeT = 0.22 which corresponds to fO_2 of about +1 to 1.5 log

242   units above FMQ (see Brounce et al., 2015).

243

244   **Sample compositions and classification**

245   We first establish lithology on the basis of whole-rock chemistry using a subset of

246   Expedition 352 whole-rock analyses (Reagan et al. 2015) for which we have corresponding thin

247   sections. The whole-rock analyses are used to classify magma types and calculations of the

248   mineral-melt equilibria. Shipboard analyses were carried out using ICP-AES methods provided

249   in Reagan et al. (2015). The effect of seawater alteration on whole rock compositions is typically

250   limited to the addition of K and in some cases Ca and Na to the whole-rock (Shervais et al.,

251   2019), which has minimal effect on the thermobarometry calculations.

252   On the basis of whole-rock geochemistry, Expedition 352 lavas are divided into basalt-

253   andesite-dacite-rhyolite and boninite series lavas on the basis of SiO_2 vs. MgO and MgO vs.

254   TiO_2 (Figures 2a, b). Boninites are further divided into basaltic boninite, low-Si boninite, and

255   high-Si boninite on this plot based on approximate liquid lines of descent for primitive boninite

256   with varying SiO_2 concentrations (Pearce and Reagan, 2019). Highly differentiated boninite plots

257   as high-Mg andesite (Figure 2). The lavas from sites U1440 and U1441 all plot as basalts within

258   the basalt-andesite-dacite-rhyolite field, whereas lavas from sites U1439 and U1442 plot as

259   various types of boninite and high-Mg andesite.

11

260   Sample 352-U1439C-8R-2-W 105/107-TSB-TS_93 from boninite Site U1439, which is

261   referred to as a high-Mg andesite below, is anomalous in that it plots within the basalt-andesite-

262   dacite-rhyolite field series on the SiO_2 vs MgO plot, but has low TiO_2 concentrations, which are

263   more akin to those of high-Mg andesite.

RESULTS

Petrography

266   The mineralogy and modal proportions of FAB, high-Mg andesite, and boninite are

267   summarized in Table 1 and their principal petrographic characteristics are presented in Table 2.

268   Representative thin section photographs are provided in Figure 3.

269   The FAB are generally aphyric with quench plagioclase, augite, and magnetite. Rare

270   plagioclase and augite phenocrysts are present in some samples, the latter of which are almost

271   always unzoned. Boninites are generally porphyritic. Low-Si boninites typically have

272   phenocrysts of olivine, Cr-spinel, and clinopyroxene, sometimes with orthopyroxene.

273   Groundmass often has quench clinopyroxene and plagioclase crystals. The high-Si boninites

274   typically contain orthopyroxene ± olivine with Cr-spinel with quench orthopyroxene and

275   clinopyroxene. Olivine crystals typically are subhedral to anhedral, whereas pyroxenes,

276   plagioclase, and Cr-spinel are typically euhedral. In most boninites, olivine, clinopyroxene and

277   orthopyroxene phenocrysts are strongly zoned. The high-Mg andesites typically have augite ±

278   orthopyroxene ± plagioclase and rare olivine phenocrysts with quench clinopyroxene and

279   plagioclase in the matrix. Detailed petrographic descriptions are provided in the supplementary

280   material[1].

281

Mineral compositions

12

283   The compositional data of all minerals are provided in the Supplementary Document

284   (Supplementary Tables S2-S7).

285   **Olivine**. EPMA analyses of olivine in the boninite are provided in Supplementary Table

286   S4. Olivine phenocrysts are highly magnesian ranging from Fo_{88} to Fo_{92} in the low-Si boninite

287   and from Fo_{87} to Fo_{93} in the high-Si boninite. Apart from one rim of olivine in a low-Si boninite

288   which has 0.15 wt.% NiO, the remaining olivine NiO contents are high (0.22-0.43wt.%),

289   approaching those of mantle olivine (cf. Sato, 1977; Takahashi et al., 1987). CaO concentrations

290   are low (0.13 to 0.20 wt%) and similar to those of olivine from water-rich subduction-related

291   basalts (Gavrilenko et al., 2016).

292   **Clinopyroxene.** 118 analyses were acquired on clinopyroxene spanning all lithologies

293   from all holes. Clinopyroxene analyses are provided in Supplementary Table S2 and Figure 4a

294   summarizes their compositional variation. All clinopyroxene in FAB, andesite, and high-Mg

295   andesite are augite, with FAB clinopyroxene extending to more Fe-rich compositions

296   ($Wo_{25}En_{44}Fs_{31}$ to $Wo_{42}En_{41}Fs_{18}$) compared with those from high-Mg andesite ($Wo_{34}En_{51}Fs_{15}$ to

297    $Wo_{42}En_{46}Fs_{12}$). Clinopyroxene from low-Si boninite vary primarily in terms of Mg and Ca,

298   ranging from $Wo_{16}En_{71}Fs_{13}$ to $Wo_{43}En_{47}Fs_{10.}$ Clinopyroxene from high-Si boninite are also augite

299   ($Wo_{27}En_{56}Fs_{17}$ to $Wo_{48}En_{30}Fs_{22}$).

300   Clinopyroxene Al_2O_3 concentrations range from 2.10-7.68 wt.%, 0.99-11.89 wt.% and

301   1.58-4.62 wt.% in the low-Si boninite, high-Si boninite and high-Mg andesite respectively.

302   Cr_2O_3 in the same order, ranges from 0.02-0.78 wt.%, 0.01-0.38 wt.% and 0.01-0.56 wt.%. FAB

303   clinopyroxene have Al_2O_3 and Cr_2O_3 which range from 1.39-7.69 wt.% and 0-0.75 wt.%,

304   respectively. In general, TiO_2 contents of the Ca-rich pyroxene are variable and Na_2O contents

305   are generally low (typically <0.25 wt.%).

13

306　　　　Mg#, Na$_2$O, TiO$_2$ and Cr$_2$O$_3$ contents of clinopyroxene show little systematic variation in

307　　FAB with depth (Figure 5). In general, no appreciable differences exist between the composition

308　　of clinopyroxene cores and rims at similar core depths for the FAB, although Na$_2$O

309　　concentrations are somewhat higher in microlites relative to phenocrysts at similar depths in

310　　Core U1440B. Similarly, compositions of clinopyroxenes in boninite and high-Mg andesite show

311　　little variation with depth. Exceptions include general increases in Mg# and decreases in Na$_2$O

312　　content with depth for both boninite sites.

313　　　　**Low-Ca pyroxene.** Analyses of low-Ca pyroxene are provided in Supplementary Table

314　　S3. Low-Ca pyroxenes are found in the low-Si boninite, high-Si boninite, and high-Mg andesite

315　　but not in FAB (Figure 4a). Low-Ca pyroxene in the low-Si boninite range from Wo$_1$En$_{89}$Fs$_{10}$ to

316　　Wo$_9$En$_{78}$Fs$_{13}$ and in the high-Si boninite, they range from Wo$_1$En$_{71}$Fs$_{10}$ to Wo$_5$En$_{89}$Fs$_{27}$.

317　　Orthopyroxene in the high-Mg andesite have a restricted range from Wo$_3$En$_{83}$Fs$_{14}$ to

318　　Wo$_5$En$_{77}$Fs$_{17}$. All low-Ca pyroxene are Mg-rich with X$_{Mg}$ (100En/(En+Fs)) typically >85 (the

319　　mean X$_{Mg}$ of all low-Si boninite and high-Si boninite low-Ca pyroxene is 86), although some

320　　high-Si boninite low-Ca pyroxene have X$_{Mg}$ <80. X$_{Mg}$ of low-Si boninite, high-Si boninite and

321　　high-Mg andesite low-Ca pyroxene range from 83-90, 72-90 and 82-86, respectively. Rims are

322　　richer in more iron-rich than their cores, with X$_{Mg}$ typically 1-2 lower than the cores.

323　　Orthopyroxene in the low-Si boninite, high-Si boninite and high-Mg andesite have low Al$_2$O$_3$

324　　(0.72-1.45, 0.26-1.61 and 0.92-1.90 wt.%, respectively) and TiO$_2$ (typically ≤0.06%) (Table A3).

325　　Cr$_2$O$_3$ contents range from 0.07-0.70 wt.% in the low-Si boninite, 0.05-0.90 wt.% in the high-Si

326　　boninite, and 0.22-0.46 wt.% in the high-Mg andesite.

327　　　　**Spinel**. EPMA analyses of Cr-spinel are provided in Supplementary Table S5. Cr-spinel

328　　occurs in both the low-Si boninite and high-Si boninite as reddish-brown, euhedral to subhedral

14

329   crystals usually as inclusions in olivine but are also present in the groundmass. Cr-spinel in both

330   the low-Si boninite and high-Si boninite have high Cr_2O_3 (52.8-62.8 wt.% and 55.8-62.9 wt.%,

331   respectively), which fall within the range of olivine-hosted spinel of Chichijima boninite (49-63

332   wt.% Cr_2O_3, Dobson et al., 2006). Cr# (=100*Cr/Cr+Al) are also high, ranging from 74-88 in

333   low-Si boninite Cr-spinel and from 79-86 in high-Si boninite Cr-spinel (Table A5). In general,

334   the very high Cr# of Cr-spinel reflect high Cr contents of host melts and low activities of Al.

335   Mg# of the Cr-spinel in the low-Si boninite and high-Si boninite range from 54-65 and 50-62,

336   respectively. Spinel Fe^{3+}/Fe^{2+} ranges from 0.22-0.42 in the low-Si boninite and from 0.15-0.34 in

337   the high-Si boninite. Fe^{3+} is derived by stoichiometry using the methods of Droop (1987).

338   Magnetite is the only Fe-Ti oxide present and occurs only in the FAB. A single magnetite

339   grain was analyzed and has MgO of 0.69 wt.%, MnO of 0.37 wt.% and Al_2O_3 of 2.75 wt.%, and

340   TiO_2 of 17.11 wt.%. (Supplementary Table S5).

341

342   **Feldspar.** Plagioclase is ubiquitous in FAB, the anomalous andesite 352-U1439C-8R-2-

343   W 105/107-TSB-TS_93 and the high- Mg andesite but relatively rare in the low-Si boninite and

344   absent from all but the most differentiated high-Si boninite. A total of 78 spot analyses were

345   obtained on plagioclase from the FAB; 16 spot analyses were obtained on plagioclase of the

346   anomalous andesite, high-Mg andesite and low-Si boninite. The compositional range of

347   plagioclase from the FAB nearly encompasses the compositions of plagioclase from all other

348   magma types, but extends to higher An content (FAB plagioclase cores record An_{51-91} with a

349   mean of An_{68}) (Figure 4b, Supplementary Table S6). For comparison, the range and mean of An

350   from plagioclase of the andesite, high-Mg andesite and low-Si boninite are An_{49-62} (An_{56}), An_{66-}

351   $_{76}$ (An_{73}) and An_{62-76} (An_{71}), respectively. Plagioclase cores were analyzed in FAB, the

352 anomalous andesite, high-Mg andesite, and low-Si boninite; plagioclase rims were analyzed in

353 the FAB only. In the FAB, plagioclase cores are normally zoned.

354   In the high-Mg andesite, plagioclase K_2O and FeO range from 0.03-0.04 wt.% and 0.75-

355 0.98 wt.%, respectively, whereas in plagioclase from the low-Si boninite, K_2O and FeO range

356 from 0.07-0.13 wt.% and 0.87-1.04 wt.%. FeO also ranges to much higher contents in the FAB

357 (0.35-2.38 wt.%) but FeO contents in the andesite plagioclase (0.75-0.80 wt.%) are lower than all

358 other magma types.

359

360   **Conditions of Crystallization**

361   Mineral composition data were filtered such that only those with totals between 98.5-101

362 wt.% oxides and with cations within 1% of 4 cations per 6 O (i.e. +/- 0.04) formula unit are used

363 in all pyroxenes used in thermobarometry calculations and related plots. Pressure and

364 temperature estimates are shown for those clinopyroxene phenocrysts and microlites, and

365 orthopyroxene and olivine phenocrysts that pass the test of mineral-liquid equilibrium (Rhodes

366 diagrams regions between dashed lines in Figure 6). Table 3 and Figure 7 provides a synopsis of

367 the pressure and temperature estimates obtained for all magma types using clinopyroxene and

368 orthopyroxene thermobarometry and olivine thermometry. Whole-rock compositions are used as

369 the input for the liquid in the thermobarometry calculations. Supplementary Tables S7 and S8

370 provide results of pressure-temperature estimates on the basis of clinopyroxene thermobarometry

371 and orthopyroxene thermobarometry, respectively; Supplementary Table S9 provides

372 temperature estimates on the basis of olivine thermometry. Supplementary Tables S7-9 provide

373 an explanation of the calculation of the means and ranges cited in Table 3. Uncertainties in

374   pressure and temperature estimates for all thermometers and barometers employed are ±1 kbar

375   and ±30°C, respectively.

376

377   **Olivine-liquid thermometry.** Most boninites from Expedition 352 have Mg#s of 80 to

378   83, which are too high to be in equilibrium with analyzed olivine crystals or for magmas in

379   equilibrium with even highly-depleted, Fo_{92}-bearing mantle (assuming $Kd_{Mg/Fe}$ between olivine

380   and melt = 0.3 and melt Fe^{3+}/FeT = 0.22) (Figure 6c, Supplementary Table S9). To adjust our

381   boninite whole rock compositions towards equilibrium, as much as 22 % accumulated olivine

382   was subtracted from both low-Si and high-Si boninites. These adjusted whole rock compositions

383   have Mg#s in the range of 0.71-0.78, which are in keeping for magmas produced from depleted

384   mantle (e.g., Roeder and Emslie, 1970). Using these adjusted melt compositions and the olivine-

385   liquid thermometry equation recommended for use when magmas are hydrous (equation 22;

386   Putirka, 2008), and assuming 2 wt% H_2O in the melt which are average values measured in

387   boninite pillow rind glasses from Chichijima (Dobson O'Neil, 1987), the low- and high-Si

388   boninites yield similar ranges of calculated temperatures (1,119-1,202) °C.

389   A geohygrometer based on the distribution coefficient of CaO between magmas and

390   olivine ($D_{CaO}^{Ol/L}$), and that is accurate to approximately 1.5 wt% was recently developed by

391   Gavrilenko et al (2016). The calculated water concentrations for Expedition 352 boninites using

392   this geohygrometer are 2–4 wt% (Figure 10). Using this range of water concentrations in

393   equation 22 from Putirka (2008), results in little change to the calculated olivine-liquid

394   temperatures (i.e. using 4 wt% water results in calculated temperatures of $1,120 – 1,200^{o}C$).

395

396   **Clinopyroxene-liquid thermobarometry.** Whole-rock Mg# vs. clinopyroxene Mg#

397   relations are shown in Figure 6a for FAB, the andesite, high-Mg andesite and boninites. Eleven

398   analyses of clinopyroxene from the FAB but none from the andesite and basaltic boninite plot

399   within the equilibrium field (Figure 6a); a large number of clinopyroxene from the FAB, high-

400   Mg andesite and boninite plot below the equilibrium field suggesting that they crystallized from

401   differentiated interstitial magma.

402   The calculated temperatures of clinopyroxene phenocrysts and microlites from the FAB

403   (when $K_D(Fe-Mg)^{cpx-liq}$ = 0.27±0.3) are narrow, yielding a mean temperature of 1163 ± 14°C in

404   the range of 1142–1190°C (*n* = 13), although the estimated pressure range is relatively large

405   (0.5–4.6 kbars) (Table 3, Supplementary Table S7). Phenocryst cores and rims and microlites

406   show similar pressure and temperature estimates in accord with Scruggs and Putirka (2018). As a

407   test of equilibrium, we use Putirka (1999) to predict the clinopyroxene end-member components

408   Di+Hd (DiHd), En+Fs (EnFs), CaTs and Jd, using the liquid composition and estimated

409   temperature and pressure as input. These predicted components represent the clinopyroxene

410   composition that should precipitate if the liquid used as the input is saturated with clinopyroxene

411   at the given temperature and pressure conditions. The components should also sum to one. If the

412   sum is greater than one, then the system is oversaturated in clinopyroxene, and for a system

413   where the sum is less than one, the liquid is undersaturated. These predicted components are also

414   compared to the observed components for a given clinopyroxene as calculated by Putirka (1999,

415   2008). If the components match within model error, then the pressure–temperature–composition

416   conditions are allowably within an equilibrium state and the pressure–temperature estimates are

417   assumed to be valid. These clinopyroxene also pass additional tests of equilibrium if the

418   predicted and measured end-member components (DiHd, EnFs and CaTs) match to within 2-σ

419   uncertainties (Supplementary Figure S1a).

420   We also calculated crystallization temperatures of clinopyroxene in equilibrium with

421   MORB (Figure 8) for comparison with FAB crystallization temperatures. The mean and range of

422   PetDB MORB (n = 75) temperatures are 1182 ± 15 °C and 1133–1240°C (Table 3,

423   Supplementary Table S10). The mean MORB temperature is close to that obtained on

424   clinopyroxene from Expedition 352 FAB (1163 ± 14°C) (Figure 9a). Pressure estimates obtained

425   from clinopyroxene in the Expedition 352 FAB (mean and range of 2.4 ± 0.4 kbar and 0.5-4.6

426   kbar) are also similar to those calculated for the PetDB MORB dataset (mean and range of 1.4 ±

427   0.2 kbar, -1.8-8.3 kbar, Figure 9b, Table 3, Supplementary Table S10). Nonetheless,

428   crystallization temperatures of FAB relative to MORB at a given pressure are demonstrably

429   lower (Figure 9b). In contrast, melting temperatures and pressures are higher than MORB

430   (Shervais et al., 2019). A plot of observed versus predicted clinopyroxene components of the 75

431   PetDB MORB samples demonstrates that the data are as robust (Supplementary Figure S1b) as

432   that of our clinopyroxene data from the Expedition 352 FAB (Supplementary Figure S1a).

433

434   **Orthopyroxene-liquid thermobarometry.** Whole rock Mg# vs. orthopyroxene Mg#

435   relations are shown in Figure 6b for the high-Mg andesite, low-Si boninite and high-Si boninite.

436   Several orthopyroxenes from the high-Mg andesite, low- Si boninite and high-Si boninite fall

437   within the orthopyroxene-basaltic melt equilibrium field.

438   Calculated orthopyroxene-melt equilibrium pressures and temperatures for Expedition

439   352 high-Mg andesite, low-Si boninite and high-Si boninite (FAB have no orthopyroxene) are

440   given in Table 3. Mean pressure and temperature estimates for the single high-Mg andesite

19

441   provide 0.2 ± 0.05 kbar and 1193 ± 26ºC (Table 3), respectively. P-T conditions determined for

442   the low-Si and high-Si boninites based on orthopyroxene thermobarometry are 0.3 ± 0.1 kbar

443   (mean) and 1214 ± 13ºC (mean) and 0.2-0.4 kbar (mean of 0.3 ± 0.1 kbar) and 1235-1264ºC

444   (mean of 1249 ± 13ºC), respectively (Table 3, Supplemental Table S8).   The temperatures

445   calculated for orthopyroxene are higher than those calculated for olivine from the low-Si

446   boninite and high-Si boninite, which agree with each other within the uncertainties of the

447   calculations (see Table 3). As orthopyroxene normally follows olivine in the boninite liquid lines

448   of descent (Pearce and Reagan, 2019), the higher calculated orthopyroxene temperatures are

449   surprising. Possible reasons for the higher boninite orthopyroxene crystallization temperatures

450   are discussed in the Discussion (P-T evolution of FAB and boninite).

451   **Inferences from spinel compositions.** Plots of TiO_2 vs. Cr# (cationic Cr/Cr+Al) and

452   TiO_2 vs. Al_2O_3 of olivine-hosted chromite of the low-Si boninite and high-Si boninite,

453   demonstrate their very low, arc-like TiO_2 and Al_2O_3 and high Cr# relative to MORB spinel

454   (Figures 11a, b). A plot of Cr# vs. Mg# in chromite demonstrates a compositional overlap of

455   low-Si boninite and high-Si boninite chromite with Izu-Bonin (Leg 125; van der Laan et al. 1992)

456   and Chichi-jima (Umino, 1986; Yajima and Fujimaki 2001) boninite spinel, and a close

457   similarity between Expedition 352 boninite spinel and boninite spinel from the Semail ophiolite

458   (Figure 11c) (Ishikawa et al. 2002).

459   A plot of Cr# vs. TiO_2 wt.% for chromite with vectors showing melt-rock reactions

460   between refractory mantle compositions and melts generated by partial melting of these sources

461   (Pearce et al., 2000) is shown in Figure 12. MORB composition melts have relatively high Al/Cr

462   ratios and high TiO_2, whereas boninite-related melts are more refractory, with low Cr/Al ratios

463   and lower TiO_2. This plot demonstrates that chromite of the Expedition 352 low-Si and high-Si

20

464   boninites overlap with the field of chromite in other IBM boninites (see Pearce et al., 2000 for

465   references) in Cr# vs. TiO_2 wt.% space. The Expedition 352 spinel also plot at the end of the

466   melt-mantle interaction trends that characterize the drilled harzburgites from Conical seamount

467   in the IBM forearc. Thus, the compositions of Expedition 352 chromite support the genetic link

468   between boninites and depleted mantle lithosphere in the forearc (Parkinson et al., 1998).

469   Dare et al. (2009) used spinel compositions to calculate fO_2 using the method of Balhaus

470   et al. (1991), and demonstrated that chromite from MORB, island arc basalts and subduction

471   initiation boninites can be discriminated on plots of $\Delta \log fO_2$ FMQ (fayalite-magnetite-quartz) vs.

472   Cr#. Compared to MORB spinel, island arc spinel were shown to have higher fO_2 and similar-to-

473   higher Cr#, reflecting the fact that fluid-rich oceanic subduction environments typically lead to

474   more oxidizing conditions and higher degrees of melting than ocean ridges. Boninites were

475   shown to have higher Cr# than both MORB and island arc basalts, and oxygen fugacities that

476   span MORB and arc values reflecting prior mantle depletion and variable fO_2 in subduction

477   components.

478   Our oxygen fugacity data reported in Supplementary Table S11 are plotted in Figure 13

479   together with the fields from Dare et al. (2009). Although the errors are high for calculated fO_2

480   ($Fe^{3+}/\Sigma Fe$ values were not quantified using Mössbauer spectrometry), the Expedition 352

481   boninites plot in the center of the boninite field with no overlap into other fields. Specifically,

482   boninites exhibit $\Delta \log fO_2$ FMQ of 0.1-1.1 with no significant differences between low and high-

483   Si varieties. Despite their lower precision, these fO_2 values are mostly within the range of c. 0.3-

484   1.5 obtained from Fe^{3+}/Fe^{2+} measurements on glasses from FAB and (younger) boninites from

485   the IBM system (Brounce et al., 2015). The high Cr# and moderately high calculated fO_2 values

21

486   for chromite from Expedition 352 boninites are similar to those of ophiolitic boninites (e.g. Dare

487   et al., 2009).

488

489   **DISCUSSION**

490   ***P–T* Evolution of FAB and boninite**

491   A plot of Mg# of FAB and MORB clinopyroxene vs. temperature estimates (Figure 9)

492   shows that FAB clinopyroxene crystallize at 1142-1190°C within the range of MORB (1133-

493   1240°C), but at slightly higher pressure (~0.2-0.5 kbar) than MORB (Figure 9b), which is at the

494   edge of model uncertainty.

495   The olivine-liquid data in Figure 7 demonstrate that the crystallization temperatures for

496   relatively primitive boninites (1,119 – 1,202^{o}C, with means and standard deviations of 1172

497   ±23°C and 1152±24°C for the low-Si boninites and high-Si boninites respectively) overlap with

498   clinopyroxene crystallization temperatures for somewhat more differentiated FAB (1142-

499   1190 °C with a mean of 1163±14 ^{o}C; (Table 3). Clinopyroxene in FAB, however, record higher

500   pressures (0.5-4.6 kbar with a mean of 2.4±0.4 kbar) than for orthopyroxene crystallization in the

501   boninites (0.2-0.4 kbar with a mean of 0.3±0.1 kbar) (Table 3). These calculations infer that FAB

502   crystallization began at marginally higher temperatures and occurred over a broader range of

503   pressures compared with boninites, which is consistent with higher P-T conditions calculated for

504   FAB generation compared with boninite (Shervais et al., 2019; Lee et al., 2009).

505   We estimate density of the FAB and boninite in order to assess relative rates of magma

506   ascension to better understand why the FAB and boninite exhibit different crystallization

507   pressures (lower for the latter with slightly lesser temperatures). We estimate density for the

508   cases of dry and hydrous compositions (FAB with 0.3 wt.% dissolved H_2O and boninite with 3

509   wt.% dissolved H_2O) using the models of Lange and Carmichael (1990) and Ochs and Lange

510   (1999), respectively, which make use of the major oxide composition of a liquid. Boninites have

511   significantly higher concentrations of MgO (9.00-16.34 wt. %) compared with FAB (5.40-8.35

512   wt. %), causing the boninites to be less dense (calculated dry and wet densities of 2.65-2.69 g/c^3

513   and 2.46-2.50 g/cm^3 for the low-Si boninites and 2.59-2.68 g/c^3 and 2.41-2.49 g/cm^3 for the

514   high-Si boninites) compared with FAB (dry density of 2.70-2.77 g/c^3 and wet density of 2.68-

515   2.74 g/cm^3) (Table 4). On the basis of differences in pressure and hence depth of formation of

516   FAB magma at ~14-16 kbar or 47-53 km (Shervais et al., 2019) and pressure and depth of

517   crystallization of the FAB (0.5-4.6 kbar or 2-15 km), the FAB magma travelled about 30-50 km

518   before crystallizing clinopyroxene. In contrast, taking into consideration the pressure and depth

519   of boninite magma formation (assuming 3 wt. % water) at 4-12 kbar or 13-40 km (Shervais et al.,

520   in preparation) and the pressure and depth of boninite crystallization at 0.2-0.4 kbar or 0.7-1.3

521   km, the boninite magma travelled between about the same distance before crystallizing

522   orthopyroxene. The presence of water lessens the density of silicate melts due to it low

523   molecular weight (Lange, 1994) and under similar magma network conditions (e.g., melt

524   conduit/pipe diameter or dike width, and wall rock density), less dense melts will ascend faster

525   than denser ones (e.g., Tanaka et al., 2014). The lesser density of the boninite relative to the FAB

526   is consistent with the former being more buoyant. In addition to a significantly shorter travel

527   time from place of magma generation to site of crystallization, the lower density allowed the

528   boninite to rise faster and to shallower levels and erupt more rapidly, thus preserving the

529   temperatures of their near-primary magmas (Table 3). It should be noted, however, that most

530   Exp. 352 boninites analyzed here erupted with accumulated crystals adding to boninite density

531   and making it less eruptible. However, olivine and pyroxenes tend to be approximately 20%

23

532   more dense than their basalt parent, so if a rock contains 10-20% olivine phenocrysts, the

533   fractional increase in density is only 0.02-0.04, which would not significantly affect density and

534   hence ascent and eruptibility, particularly as the boninite magmas were volatile saturated and

535   with bubbles relative to the FAB magma. Significant density differences between the FAB and

536   boninite thus suggests that the latter rose faster from their source than FAB thus preserving

537   relatively high crystallization temperatures.

538   The average mantle separation temperature for FAB (the last temperature of magma-

539   mantle equilibration) is 1,380^{o}C at 15 kbar (Shervais et al., 2019) and our calculated

540   clinopyroxene temperatures are 1179°C at 4.6 kbar to 1142°C at 0.5 kbar (Supplementary Table

541   S8). Thus, the cooling rate for the shallow part of the system (9.02^{o}C/kbar or about 2.72^{o}C/km) is

542   about half that calculated for magma to get from its source at 15 kbar to 4 kbar (19.3^{o}C/kbar or

543   5.9^{o}C/km), which may be the result of latent heat release during crystallization at crustal

544   pressures. Low-Si boninite, however, typically last equilibrated with mantle at 0.8 kbar and

545   1270°C with 3 wt.% water (Shervais et al., in preparation). Our olivine crystallization

546   temperatures record fractionation starting at 1202°C (Supplementary Table S10) and our

547   orthopyroxene barometry suggests fractionation at 0.3 kbar (Table 3). This yields a rapid cooling

548   rate of greater than 100°C/kbar or >30°C/km, significantly higher than for FAB. However, the

549   calculated orthopyroxene crystallization temperatures of 1214°C for the low-Si boninite and

550   1235-1264°C for the high-Si boninite (Table 3, Supplementary Table S8), suggest that

551   crystallization histories for the boninites are complex.

552   The increase in crystallization temperature for boninite orthopyroxene relative to boninite

553   olivine is surprising as the former follows the latter in the liquid line of descent for boninite

554   (Pearce and Reagan, 2019) and so is expected to yield a lower crystallization temperature. The

555 significant temperature increase indicates a significant contribution of latent heat to the thermal

556 budget which could be the result of for example, a heating event by hotter, more mafic magma

557 just prior to eruption (e.g., Venezky and Rutherford, 1999; Devine et al., 2003). Alternatively,

558 Blundy et al. (2006) argued that temperature increase in Mount St. Helen and Shiveluch

559 (Kamchatka, Russia) andesitic magmas were caused instead by latent heat release of

560 crystallization via magma decompression and degassing, which they contend is likely in any

561 hydrous magma that decompresses at a rate that permits crystallization and heat retention. This

562 may be the case in the Exp. 352 boninite (Fig. 15).

563

564 **Comparison of crystallization temperature and pressure with other IBM boninites**

565 Expedition 352 boninites record crystallization temperatures similar to those of other Izu-

566 Bonin boninites. Expedition 352 low-Si and high-Si boninite olivine temperature estimates

567 (means of 1172 ± 23°C and 1152 ± 24° C, respectively) and orthopyroxene temperature

568 estimates (means of 1214 ± 9°C and 1249 ± 13° C, respectively) fall within the temperature

569 range obtained via pyroxene thermometers on boninites (1080-1287°C, Dobson et al. 2006;

570 Supplementary Table S12) from Chichijima (~160 km SSW of Expedition 352 Sites). The range

571 of <1100-1260°C calculated via phase relations for Izu-Bonin forearc (Site 786, Ocean Drilling

572 Program) boninites by van der Laan et al. (1992) also encompasses the range in temperatures

573 estimated for Expedition 352 low-Si boninites on the basis of orthopyroxene thermometry, and

574 high-Si boninites on the basis of orthopyroxene and olivine thermometry within the uncertainties

575 (Table 3, Supplementary Table S12). Thus, temperatures largely overlap for all boninites from

576 the Bonin Islands region.

577

578 **Comparisons of FAB to MORB and the Semail ophiolite**

REVISION 5

579   Here, we compare our results for the IBM forearc lavas with MORB and ophiolites to test

580   the hypothesis that the birthplace of ophiolites is a proto-arc/forearc environment formed during

581   subduction initiation. Such data also illustrate changes in conditions of magma differentiation as

582   the geodynamics of volcanism evolved after subduction initiation. First, we use discrimination

583   diagrams for FAB (below) and then boninites (next section) to compare conditions of

584   crystallization with lavas from known tectonic settings.

585   In the Oman ophiolite, initial MORB-like lavas (lower Geotimes Unit) were followed by

586   the eruption of arc-like basalts (Lasail and Alley units; Alabaster et al., 1982). The time

587   progression from less LILE-depleted and HFSE-enriched lavas to LILE-enriched and HFSE-

588   depleted compositions defines the subduction initiation rule of Whattam and Stern (2011) and is

589   characteristic of other ophiolites, e.g., Mirdita (Dilek et al., 2008) and Pindos (Saccani and

590   Photiades, 2004) and the Central American forearc (Whattam et al., 2020). In Figure 16a we

591   show that 93% of the clinopyroxene from Expedition 352 FAB plot to the right (high TiO_2 side)

592   of a line of $Cr_2O_3 = (5.28 \times TiO_2) -2.62$ drawn here to separate FAB from boninite (more

593   depleted melt compositions lie left of the line). The Expedition 352 FAB clinopyroxene plot

594   along with 97% of MORB ($n = 1198$) whereas 81% of the boninite clinopyroxenes plot to the

595   left of this line. We take the decrease in Ti and increase of Cr concentrations in clinopyroxene

596   from lower FAB to upper FAB and boninite to be a reflection of the concentrations of these

597   elements in their associated melts, which suggests increasing depletion of the magma sources

598   with time. All of the MORB-like Geotimes Unit basalts of Oman plot to the right of the line of

599    $Cr_2O_3 = (5.28 \times TiO_2) -2.62$ and the majority of the arc-like Alley Unit (79%) plot to the left of

600   this line (Figure 16b) indicating a similar increased depletion with stratigraphic height. The plot

601   does not effectively discriminate the arc-like Lasail Unit of Oman, however, as 79% of lavas of

26

602   this unit plot with the FAB and MORB and 65% of lavas of the arc-like cpx-phyric unit plots to

603   the left of the line with the Alley Unit lavas.

604

605   **IMPLICATIONS FOR OPHIOLITE AND FOREARC CRUST FORMATION**

606   Originally interpreted as 'trapped' West Philippine Basin back arc basin crust generated

607   prior to subduction inception (DeBari et al. 1999, see Figure 1 for location of their study), FAB

608   were instead interpreted by Reagan et al. (2010) as the first lavas formed after subduction

609   initiation as the result of decompression melting of the mantle during forearc spreading (Kodaira

610   et al., 2010). This model is similar to that first proposed by Stern and Bloomer (1992) and that

611   was later refined to include ophiolite petrogenesis by Shervais (2001), Whattam and Stern (2011)

612   and Stern et al. (2012).

613   On the basis of clinopyroxene thermobarometry and chemistry from this study, the FAB

614   exhibit mostly MORB-like tectonomagmatic affinities with crystallization pressures and

615   temperatures on the high-P, low-T side of the MORB array. These findings lend credence to the

616   idea of an origin for FAB by sea-floor spreading, albeit above a newly subducting slab (e.g.,

617   Reagan et al., 2010; Shervais et al., 2019), which may explain the steeper trajectory of cooling

618   for FAB relative to MORB.

619   We suggest that, in the case of the present study area, initial partial melting of previously

620   depleted mantle (Yogodzinski et al., 2018; Li et al., 2019) during seafloor spreading at source

621   depths lower than those of MORB (46-53 km vs. ~60-80 km), and at higher temperatures

622   (Shervais et al., 2019) produced FAB (Fig. 17). The unusually high temperatures of melting to

623   generate FAB might have originated in the Manus Plume, which has been interpreted to have

624   surfaced in the Bonin island region about the time of subduction initiation (Macpherson and Hall

27

625   2001; Wu et al., 2016; Shervais et al., 2018). Following extraction of the FAB, the highly

626   depleted residual harzburgitic mantle remained in the mantle wedge and was fluxed by slab-

627   derived fluids. Boninitic magmas were then generated at low pressure possibly via partial

628   melting of diapirs of slab-metasomatized residual MORB mantle. A similar chemotemporal

629   model has been proposed for the Oman ophiolite (Alabaster et al., 1982) and could be a model

630   for many supra-subduction zone ophiolites as summarized by Whattam and Stern (2011).

631   The Expedition 352 FAB pre-date boninite formation by no more than 0.6 m.y. (Reagan

632   et al., 2019), which is similar to the rapid time-frame of magma sequences in ophiolites (e.g.

633   Rioux et al. 2012). Results of this study corroborate a similar chemo-temporal progression of the

634   Izu-Bonin forearc with subduction initiation ophiolites. This in turn implies similar origins for

635   the IBM forearc and "subduction-initiation rule" (Whattam and Stern, 2011) ophiolites. The

636   chemo-temporal transition from FAB to boninite in lavas of both ophiolites and the Izu-Bonin

637   forearc have been interpreted to reflect a dynamic, tectonic setting with rapidly changing

638   conditions of magma genesis that accompany the deepening of the slab and evolution of slab-

639   derived fluid pathways over the course of subduction initiation (Whattam and Stern, 2011; Stern

640   et al., 2012). Such a progression is becoming increasingly apparent for ophiolites (e.g., Shervais,

641   2001; Pearce and Robinson 2010; Whattam and Stern 2011; Stern et al. 2012; Moghadam et al.

642   2014) and other intra-oceanic forearcs (e.g., Torro et al., 2017; Whattam et al., 2020) on a global

643   scale.

644

28

657

658   **Figure Captions**

659   Fig. 1 Study areas. (a) Geological setting of the Izu-Bonin Mariana arc system in the western

660   Pacific. The circled numbers 1, 2, and 3 represent active spreading ridges, extinct spreading

661   ridges and convergent margin or trenches (i.e., subduction zones), respectively; the boxes

662   labelled 'Dive area A' and 'Dive area B' to the immediate east of the Izu-Bonin Arc and Guam

663   represent the regions in which the dive sites of DeBari et al. (1999) and Reagan et al. (2010)

664   respectively, were conducted as discussed in the text. (b) Location of Expedition 352 drill sites to

665   the immediate NE of the Bonin Islands. Box above, magnification of Sites U1439, U1442,

666   U1440 and U1441 (filled yellow circles) shown in main figure. The boxes labelled 'Dive area

667   C1, C2, and C3' represent the dive sites of Ishizuka et al. (2011) as discussed in the text.

668   (c) Two alternative interpretations of the stratigraphic section (not to scale) of the Bonin forearc

669   drill site area. Interpretation I (top) entails FAB underlying boninite whereas the second one

670   (bottom) entails FAB lying 'trenchward' and the boninite lying 'arcward'. The bottom panel

671   (second interpretation) is from Reagan et al. (2015).

672

673   Fig. 2 Whole rock classification of Expedition 352 lavas. (a) MgO vs. SiO_2 of Expedition 352

674   magmas. The IUGS classification of boninites (grey shade) in (a) and (b) is from LeBas (2000).

675   The boundaries between basalt-andesite-dacite-rhyolite (BADR) series and boninite series is

676   from Pearce and Robinson (2010) and the subdivision of boninites into basaltic boninites (BB),

677   low-Si boninites (LSB) and high-Si boninites (HSB) is from Reagan et al. (2015). The formal

678   IODP number for TS 93 is 352-U1439C-8R-2-W 105/107-TSB-TS_93.

679

680   Fig. 3 Photomicrographs of representative Expedition 352 lavas. a, b) FAB (TS 50), (c, d)

681   anomalous andesite (TS 93), (e, f) high-Mg andesite (TS 208), (g, h) low-Si boninite (TS 111),

682   and (i, j) high-Si boninite (TS 185) under (a, c, e, g, i) plane polarized light and (b, d, f, h, j)

683   cross polarized light. Scale bar in the lower right of each image is 1000 μm (1 mm). Formal

684   IODP numbers for TS 50, TS 93, TS 208, TS 111 and TS 185 are shown on the bottom left-hand

685   side of the plane polarized images and all formal IODP numbers are provided in Supplementary

686   Table 1.

687

688   Figure 4 Mineral classification of Expedition 352 lavas. (a) FAB, anomalous andesite (TS 93),

689   high-Mg andesite and boninite clinopyroxene and orthopyroxene classification based on the En-

690   Fo-Ws pyroxene quadrilateral (Morimoto, 1998). The large spread in compositions of

691   clinopyroxene is related to quench effects on rims and small grains. The large and small symbols

692   represent cores and rims, respectively. (c) FAB, andesite, high-Mg andesite and low-Si boninite

693   plagioclase classification.

694

695   Fig. 5 Expedition 352 clinopyroxene composition vs. sub-seafloor depth. Forearc basalt,

696   andesite, high magnesium andesite and boninite clinopyroxene Mg# (cationic Mg/Mg+Fe^{2+}),

697   Na$_2$O, TiO$_2$ and Cr$_2$O$_3$ vs. depth in meters below sea floor (mbsf). Note that in the Na$_2$O vs.

698   depth plot, five forearc basalt clinopyroxenes (154 m depth) plot off the right of the plot with

699   anomalously high Na_2O ranging from 1.93-2.49 wt.% and that in the TiO_2 vs. depth plot, two

700   forearc basalt clinopyroxenes plot off the right of the plot with anomalously high TiO_2 of 1.22

701   and 1.89 wt.%.

702

703   Fig. 6 Mineral-melt Fe/Mg equilibrium diagrams for Expedition 352 lavas. (a) clinopyroxene, (b)

704   orthopyroxene and (c) olivine of FAB, andesite, high-Mg andesite and boninite varieties. In a-c,

705   the Mg# is calculated assuming Fe^{3+}/Fe^{2+} =0.17 of FeT and the equilibrium fields are represented

706   by the gray shaded region (Rhodes diagram). In (a), the equilibrium field for Fe/Mg exchange

707   between clinopyroxene and basaltic melt is 0.23±0.05, (Toplis and Carroll, 1995). In (b), the

708   equilibrium field for Fe/Mg exchange between orthopyroxene and basaltic melt is 0.29±0.06

709   (Rhodes et al., 1979). In (c), the equilibrium field for Fe/Mg exchange between olivine and

710   basaltic melt is 0.30±0.03 (Roeder and Emslie, 1970). The Mg# of the whole rocks was corrected

711   by olivine subtraction so that the samples lie along the equilibrium curve

712

713   Fig. 7 Pressure-temperature summary plot. Plot shows the mean estimated pressures and

714   temperatures calculated via clinopyroxene and orthopyroxene thermobarometry and olivine

715   thermometry. Uncertainties in the pressure and temperature estimates are ±1 kbar and ±30°C,

716   respectively. Abbreviation: tb (beside cpx and opx), thermobarometry.

717

718   Fig. 8 Mineral-melt Fe/Mg equilibrium diagram for PetDB MORB clinopyroxenes. The

719   equilibrium field for Fe/Mg exchange between clinopyroxene and basaltic melt is 0.27±0.03,

720   (Toplis and Carroll, 1995) and is represented by region enclosed by dashed lines (Rhodes

721   diagram).

722

723   Fig. 9 Temperature vs. Mg # and pressure of Expedition 352 FAB clinopyroxene vs. MORB

724   clinopyroxene. In (a) and (b) means only are plotted; standard deviations are provided in Table 3.

725   In (b) the larger white circles enclosing a smaller purple and grey circle represent the mean

726   temperature and pressure estimates of Expedition 352 FAB and MORB clinopyroxenes,

727   respectively. Note also in (b) that one PetDB MORB sample (MELPROT-5-037-001) plots off

728   the top of the figure with a P of 8.3 kbar and temperature of 1188°C. See Table 3 and

729   supplementary material[1] for details of calculation of FAB and MORB clinopyroxene temperature

730   estimates.

731

732   Fig. 10 Geohygrometer based on the distribution coefficient of CaO between magmas and

733   olivine ($D_{CaO}^{O/L}$) vs. MgO of Exp. 352 boninite which is accurate to approximately 1.5 wt%

734   (Gavrilenko et al (2016).

735

736   Fig. 11 Tectonomagmatic discrimination of Expedition 352 boninites on the basis of chromian

737   spinel composition. (a) Chromian number (Cr#, cationic Cr/Cr+Al) vs. TiO_2 (Arai, 1992), (b)

738   Al_2O_3 vs. TiO_2 (Kamenetsky et al., 2001) and (c) Mg vs. Cr# number of boninite spinel

739   inclusions in olivine. Shown for comparison in (c) are the fields of boninite spinel compositions

740   of (1) the Mariana forearc (Bloomer and Hawkins, 1987), (2) Chichijima (Umino, 1986; Yajima

741   and Fujimaki, 2001), (3) of the Izu-Bonin forearc (Leg 125, van der Laan et al., 1992), (4) the

742   Semail ophiolite (Ishikawa et al., 2002) and (5) the Troodos ophiolite (Cameron, 1985).

743

744   Fig. 12 Spinel Cr# vs. TiO$_2$ relations of Expedition 352 boninites. The plot (Pearce et al., 2000)

745   demonstrates that Expedition 352 boninites overlap with the field of Cr-spinel in other IBM

746   boninites (see Pearce et al., for references) and supports the model in which some boninite melts

747   also refertilize the forearc mantle lithosphere upon ascent to the surface (Parkinson et al., 1998).

748

749   Fig. 13 Plot of Δlog fO$_2$ FMQ (fayalite-magnetite-quartz) vs. spinel Cr# (Dare et al., 2009) of

750   Expedition 352 boninites. fO$_2$ is calculated by the method of Balhaus et al. (1991).

751   Supplementary Table S12 gives values and errors.

752

753   Fig. 14 Depth vs. density of FAB and boninite assuming 0.3 wt.% and 3 wt.% dissolved H$_2$O in

754   the FAB and boninite magma, respectively. Error bars represent ± 1 standard deviation. In all

755   cases, the uncertainty of the error is smaller than the symbol size. Densities were calculated from

756   Ochs and Lange (1999).

757

758   Fig. 15 SEM-BSE images of resorbed olivine in Exp. 352 high-Si boninite. (a) Sample U1439A

759   21X-CC 22/25. Resorbed olivine (with chromite inclusions). This olivine has a very thin Fe-rich

760   rim suggesting that olivine started to grow again from the melt about the time of cooling

761   associated with eruption. This texture may be explained by olivine growth from primitive high-Si

762   boninite, resorption by heating during rapid orthopyroxene growth, followed by saturation at the

763   end during eruption as the system cooled (b) Sample 352-U1439C-5R-1-W 92/95-TSB-TS_88.

764   Our interpretation is that olivine first grew from a melt that became more magnesian probably

765   due to mixing with a more mafic magma. This was followed by resorption and orthopyroxene

766   growth on the resorbed olivine. We interpret this olivine resorption to possibly be the result of

767 heating due to early orthopyroxene growth (note the composition of the orthopyroxene

768 immediately surrounding the olivine which is the same as the outer zone (spot 6) of the nearby

769 orthopyroxene to the left).

770

771 Fig. 16 Subdivision of Expedition 352 FAB and boninites vs, Semail ophiolite lavas on the basis

772 of clinopyroxene Cr_2O_3 vs. TiO_2 relations. (a) Expedition 352 FAB and (b) Semail ophiolite

773 lavas (Alabaster et al., 1982).The sub-vertical line is $Cr_2O_3 = (5.28 \times TiO_2)-2.62$.

774

775 Fig. 17 Cartoon depicting the tectonomagmatic evolution (after Reagan et al., 2017) and

776 formation and crystallization histories of the (a) FAB and (b) boninite. Formation pressure and

777 temperature constraints for the FAB and boninite are from Shervais et al. (2019) and Shervais

778 (personal communication), respectively. The boninite formation temperature is based on the

779 boninite comprising 3 wt.% H2O. The white circles encompass the range of pressure conditions

780 but because the range of pressure of crystallization of the boninite is small (0.2-0.4 kbar) its

781 circle is enlarged x 5. TF and TC = formation temperature and crystallization temperature

782 (ranges). DMM, depleted MORB mantle.

783

784 Table captions

785 Table 1 Modal estimates of phenocrysts and groundmass constituents of the FAB, lone andesite,

786 high-Mg andesites and boninites.

787

788 Table 2 Synopsis of the petrographic features of the FAB, lone andesite, high-Mg andesites and

789 boninites.

34

790

791   Table 3 Thermobarometry summary.

792

793   **REFERENCES CITED**

794   Acland, A.S. (1996) Magma genesis in the northern Lau Basin, SW Pacific. Ph.D. dissertation, Durham

795   University.

796   Alabaster, T., Pearce, J.A., and Malpas, J. (1982) The volcanic stratigraphy and petrogenesis of the Oman

797   ophiolite complex. Contributions to Mineralogy and Petrology, 81, 168-183.

798   Arai, S. (1992) Chemistry of chromian spinel in volcanic rocks as a potential guide to magma history.

799   Mineralogical Magazine, 56, 173-184.

800   Arai, S., 1994. Characterization of spinel–peridotites by olivine–spinel compositional relationships: review and

801   interpretation. Chemical Geology 113, 191–204.

802   Arai, S., Abe, N., Hirai, H., 1998. Petrological characteristics of the sub-arc mantle: an overview on petrology of

803   peridotite xenoliths from the Japan Arcs.Trends in Mineralogy 2, 39–55.

804   Arculus, R. J., and 29 others (2015) A record of spontaneous subduction initiation in the Izu-Bonin-Mariana arc.

805   Nature Geosciences. 8, 728-733.

806   Ballhaus, C., Berry, R.F. & Green, D.H., 1991. High pressure experimental calibration of the olivine-

807   orthopyroxene-spinel oxygen geobarometer: implications for the oxidation state of the upper

808   mantle. Contributions to Mineralogy and Petrology, 107, 27, https://doi.org/10.1007/BF00311183.

809   Beattie, P., 1993. Olivine-melt and orthopyroxene-melt equilibria. Contributions to Mineralogy and Petrology

810   115, 103-111.

811   Beccaluva, L., Macciotta, G., Piccardo, G.B., and Zeda, O. (1989) Clinopyroxene compositions of ophiolite

812   basalts as petrogenetic indicator. Chemical Geology, 77, 165-182.

813   Bloomer, S. H., and J. W. Hawkins (1983) Gabbroic and ultramafic rocks from the Mariana Trench; an island arc

814   ophiolite, in *The Tectonic and Geologic Evolution of Southeast Asian Seas and Islands: Part 2*,

815   Geophysical Monograph Series, vol. 27, edited by D.E. Hayes, pp. 294–317, AGU,Washington, D. C.

816   Bloomer, S.H. and Hawkins, J.W. (1987) Petrology and geochemistry of boninite series volcanic rocks from the

817   Mariana trench. Contributions to Mineralogy and Petrology, 97, 361-377.

REVISION 5

818   Bloomer, S.H., Taylor, B., MacLeod, C.J., Stern, R.J., Fryer, P., Hawkins, J.W., and Johnson, L. (1995) Early

819   arc volcanism and the ophiolite problem: a perspective from drilling in the western Pacific. In Taylor, B.,

820   and Natland, J. (Eds.), Active Margins and Marginal Basins of the Western Pacific. Geophysical

821   Monograph, 88:1–30. http://dx.doi.org/10.1029/GM088p0001.

822   Blundy, J., Cashman, K., and Humphreys, M. (2006) Magma heating by decompression-driven crystallization

823   beneath andesite volcanoes. Nature 443/776-80. doi:10.1038/nature05100.

824   Brey, G.P., and Köhler, T. (1990) Geothermobarometry in 4-phase lherzolites II. New thermobarometers and

825   practical assessment of existing thermobarometers. Journal of Petrology, 31(6), 1353-1378.

826   Brounce, M., Kelley, K.A., Cottrell, E. and Reagan, M.J. (2015) Temporal evolution of mantle wedge oxygen

827   fugacity during subduction initiation. Geology, 43, 775-778.

828   Cameron, W.E. (1985) Petrology and origin of primitive lavas from the Troodos ophiolite, Cyprus. Contributions

829   to Mineralogy and Petrology, 89, 239-255.

830   Chapman, T., Clarke, G.L., Reagan, M.J., Sakuyama, T., Godard, M., Shervais, J.W. Prytulak, J., Shimizu, K.,

831   Nelson, W., Heaton, D., Li., H., Whattam, S.A. and Pearce, J.A. (2016) A tale of phenocrysts: Trace

832   element contents of boninites and forearc basalts from IODP Exp. 352. AGU Fall Meeting, 2016.

833   Cluzel, D., Aitchison, J.C., Picard, C. (2001) Tectonic accretion and underplating of mafic terranes in the Late

834   Eocene intraoceanic fore-arc of New Caledonia (Southwest Pacific): Geodynamic implications.

835   Tectonophysics, 340, 23–59.

836   Coleman, R.G. (1981) Tectonic setting for ophiolite obduction in Oman. Journal of Geophysical Research, 86,

837   2497-2508.

838   Condie, K.C. (1989) Geochemical changes in basalts and andesites across the Archean-Proterozoic boundary:

839   Identification and significance. Lithos, 23, 1-18.

840   Cosca, M.A., Arculus, R.J., Pearce, J.A., and Mitchell, J.G. (1998) $^{40}Ar/^{39}Ar$ and K-Ar geochronological age

841   constraints for the inception and early evolution of the Izu-Bonin-Mariana arc system. Island Arc, 7(3),

842   579–595. http://dx.doi.org/10.1111/j.1440-1738.1998.00211.x.

843   Crawford, A.J., Falloon, T.J., and Green, D.H. (1989) Classification, petrogenesis and tectonic setting of

844   boninites. In: Crawford, A.J. (Ed.), *Boninites and Related Rocks*. Unwin Hyman, London, pp. 1-49.

845   Danyushevsky, L.V., Sobolev, A.V. (1996) Ferric-ferrous ratio and oxygen fugacity calculations for primitive

846   mantle-derived melts: Calibration of an empirical technique. Mineralogy and Petrology, 57, 229–241.

847   Dilek, Y., Furnes, H., and Shallo, M. (2008) Geochemistry of the Jurassic Mirdita Ophiolite (Albania)

848   and the MORB to SSZ evolution of a marginal basin oceanic crust. Lithos, 100, 174-209.

849   Dare, S.A.S., Pearce, J.A., McDonald, I., and Styles, M.T. (2009). Tectonic discrimination of peridotites using

850   fO$_2$–Cr# and Ga–Ti–Fe^{III} systematics in chrome–spinel. Chemical Geology 261, 199-216.

851   DeBari, S.M., Taylor, B., Spencer, K., Fujioka, K. (1999) A trapped Philippine Sea Plate origin for MORB from

852   the inner slope of the Izu-Bonin Trench. Earth Planet. Sci. Lett. 174, 183-197.

853   Devine, J.D., Rutherford, M.J., Norton, G.E. and Young, S.R. (2003) Magma storage region processes inferred

854   from geochemistry of Fe-Ti oxides in andesitic magma, Soufriere Hills Volcano, Monserrat, WI. Journal

855   of Petrology, 44, 1375-1400.

856   Dilek Y, Furnes, H., and Shallo, M. (2007) Suprasubduction zone ophiolite formation along the periphery of

857   Mesozoic Gondwana. Gondwana Research, 11, 453-475.

858   Dobson, P.F., Blank, J.G., Maruyama, S., and Liou (2006) Petrology and geochemistry of boninite-series rocks,

859   Chichijima, Bonin Islands, Japan. International Geology Review 48(8), 669-701. doi: 10.2747/0020-

860   6814.48.8.669.

861   Dobson, P.F., Skogby, H. and Rossman, G.R. (1995). Water in boninite glass and coexisting orthopyroxene:

862   concentration and partitioning. Contributions to Mineralogy and Petrology, 118, 414-419.

863   Droop, G.T.T., 1987. A general equation for estimating Fe^{3+} concentrations in ferromagnesian silicates and

864   oxides from microprobe analyses, using stoichiometric criteria. Mineralogical Magazine, 51, 431-435.

865   Evans, C.A., Castaneda, G. and Franco, F. (1991) Geochemical complexities preserved in the volcanic rocks of

866   the Zambales Ophiolite, Philippines. Journal of Geophysical Research, 96, 16251-16262, doi:

867   10.1029/91JB01488.

868   Falloon, T.J., and Danyushevsky, L.V. (2000) Melting of refractory mantle at 1.5, 2.0 and 2.5 GPa under

869   anhydrous and H2O-undersaturated conditions: implications for the petrogenesis of high-Ca boninites and

870   the influence of subduction components on mantle melting. Journal of Petrology, 41, p147-283.

871   Falloon, T.J., Green, D.H., and Danyushevsky, L.D. (2007) Crystallization temperatures of tholeiite parental

872   liquids: Implications for the existence of thermally driven plumes. In: Foulger, G.R., Jurdy, D.M. (Eds.),

873   Plates, plumes and planetary processes. Geological Society of America Special Paper 430, pp. 235-260.

874   doi: 10.1130/2007.2430(12).

875 Gale, A., Dalton, C.A., Langmuir, C.H., Su, Y., and Schilling, J.-G. (2013) The mean composition of ocean

876   ridge basalts. Geochemistry, Geophysics, Geosystems, 14(3), 489-518. doi:10.1029/2012GC004334.

877 Green, D.H. (1973) Experimental melting studies on a model upper mantle composition under water-saturated

878   and water-undersaturated conditions. Earth and Planetary Science Letters, 19, 37-53.

879 Green, D.H. (1976) Experimental testing of "equilibrium" partial melting of peridotite under water-saturated,

880   high-pressure conditions. Canadian Mineralogist, 14, 255-268.

881 Glennie, K.W., Boeuf, M.G., Hughes-Clarke, M.H.W., Moody-Stuart, M., Pilaar, W.F., and Reinhardt, B.M.

882   (1974) Geology of the Oman mountains. Verhandelingen Koninklijk Nederlands geologisch

883   mijnbouwkundidg Genootschap 31, 423 pp.

884 Grove, T.L., and Bryan, W.B. (1983) Fractionation of pyroxene-phyric MORB at low pressure: An experimental

885   study. Contributions to Mineralogy and Petrology, 84, 293-309.Hall, C.E., Gurnis, M., Sdrolias, M.,

886   Lavier, L.L., and Dietmar Müller, R. (2003) Catastrophic initiation of subduction following forced

887   convergence across fracture zones. Earth and Planetary Science Letters, 212(1-2):15–30.

888   http://dx.doi.org/10.1016/S0012-821X(03)00242-5.

889 Herzberg, C., and Zhang, J. (1996) Melting experiments on anhydrous peridotite KLB-1: Compositions of

890   magmas in the upper mantle and transition zone. Journal of Geophysical Research, 101, 8271-8295.

891 Hickey-Vargas, R., Yogodzinski, G. M., Ishizuka, O., McCarthy, A., Bizimis, M., Kusano, Y., et al. (2018)

892   Origin of depleted basalts during subduction initiation and early development of the Izu-Bonin-Mariana

893   Island arc: Evidence from IODP Expedition 351 Site U1438, Amami-Sankaku Basin. Geochimica et

894   Cosmochimica Acta, 229, 85-111. https://doi.org/10.1016/j.gca.2018.03.007.Hoover, J.D., Irvine, T.N.

895   (1977) Liquidus relationships and Mg-Fe partioning on part of the system $MgSi_2O_4$-Fe_2SiO_4-$CaMgSi_2O_6$-

896    $CaFeSi_2O_6$-$KaAlSi_3O_8$-SiO_2. Carnegie Institute of Washington Yearbook, 77, 774-784.

897 Irvine, T.N., and Baragar, W.R.A. (1971) A guide to the chemical classification of common volcanic rocks.

898   Canadian Journal of Earth Sciences, 8, 523–548.

899 Ishikawa, T., Nagaishi, K., and Umino, S. (2002) Boninitic volcanism in the Oman ophiolite: Implications for

900   the thermal condition during transition from spreading ridge to arc, Geology 30, 899-902.

38

901   Ishizuka, O., Kimura, J.-I., Li, Y.B., Stern, R.J., Reagan, M.K., Taylor, R.N., Ohara, Y., Bloomer, S.H., Ishii, T.,

902   Hargrove, U.S., III, and Haraguchi, S. (2006) Early stages in the evolution of Izu-Bonin arc volcanism:

903   New age, chemical, and isotopic constraints. Earth and Planetary Science Letters, 250(1–2):385–401,

904   http://dx.doi.org/10.1016/j.epsl.2006.08.007.

905   Ishizuka, O., Tani, K., Reagan, M.K., Kanayama, K., Umino, S., Harigane, Y., Sakamoto, I., Miyajima, Y.,

906   Yuasa, M., and Dunkley, D.J. (2011) The timescales of subduction initiation and subsequent evolution of

907   an   oceanic   island   arc.   Earth   and   Planetary   Science   Letters,   306(3-4),   229-240,

908   http://dx.doi.org/10.1016/j.epsl.2011.04.006.

909   Jarosewich, E., Nelen, J.A., and Norberg, J.A. (1980) Reference samples for electron microprobe analysis.

910   Geostandard Newsletter 4, 43-47.

911   Kamenetsky, V., Crawford, A.J., and Meffre, S. (2001) Factors controlling chemistry of magmatic spinel: An

912   empirical study of associated olivine, Cr-spinel and melt inclusions from primitive rocks. Journal of

913   Petrology, 2, 655–671.

914   Kelley, K.A., and Cottrell, E. (2009) Water and the oxidation state of subduction zone magmas. Science, 325,

915   605-607, doi:10.1126/science .1174156.

916   Kodaira, S., Fujiwara, T., Noguchi, N., and Takahashi, N. (2011) Structural variation of the Bonin ridge revealed

917   by modeling of seismic and gravity data. Earth Planets Space, 63, 963-973, doi:10.5047/eps.2011.06.036.

918   Kuno, H. (1968) Differentiation of basalt magmas. In: Hess, H.H., Poldervaart, A.A. (Eds.), Basalts: The

919   Poldervaart Treatise on Rocks of Basaltic Composition, 2. Interscience, New York, pp. 623–688.

920   Kushiro, I. (1972). Effect of water on the composition of magmas formed at high pressures. Journal of Petrology,

921   13, 311-334.

922   Kushiro, I. (1974). Melting of hydrous upper mantle and possible generation of andesitic magmas: An approach

923   from synthetic systems. Earth and Planetary Science Letters, 22, 294-299.

924   Kushiro, M.J.A. (2007). Origin of magmas in subduction zones: A review of experimental studies. Proceedings

925   of the Japan Academy, Series B, Physical and Biological Sciences, 83.

926   Lange, R.A. (1994). The effect of H_2O, CO_2 and F on the density of and viscosity of silicate melts. Reviews of

927   Mineralogy, 30, 331-369.

REVISION 5

928   Lange, R.L. and Carmichael, I.S.E. (1990). Thermodynamic properties of silicate liquids with emphasis on
929   density, thermal expansion and compressibility. In: Nicolls, J. and Russell, J.K. (Eds.), Modern methods
930   of igneous petrology. Mineralogical Society of America, Reviews in Mineralogy, 24, 25-64.

931   LeBas, M.J. (2000) IUGS reclassification of the high-Mg and picritic volcanic rocks. Journal of Petrology,
932   41(10), 1467-1470.

933   Leng, W. and Gurnis, M. (2015) Subduction initiation at relict arcs. Geophysical Research Letters, 42, 7014-
934   7021, doi:10.1002/2015GL064985.

935   Leterrier, J., Maury, R.C., Thonon, P., Girard, D., Marchal, M. (1982) Clinopyroxene composition as a
936   method of identification of the magmatic affinities of paleo-volcanic series. Earth and Planetary
937   Science Letters, 59, 139-154.

938   Li, Y.-B., Kimura, J.-L., Machida, S., Ishii, T., Ishiwatari, A., Maruyama, S., Qiu, H.-N., Ishikawa, T., Kato, Y.,
939   Haraguchi, S., Takahata, N., Hrahara, Y., Miyazali, T. (2013) High-Mg adakite and low-Ca boninite from
940   a Bonin fore-arc seamount: Implications for the reaction between slab melts and depleted mantle. Journal
941   of Petrology, 54, 1149-1175.

942   Lippard, S.J., Shelton, and A.W., Gass, I.G. (1986) The ophiolite of northern Oman. Oxford: Blackwell
943   Scientific Publications, 178 pp.

944   Longhi, J., Durand, S.R., and Walker, D. (2010) The pattern of Ni and Co abundances in lunar olivines.
945   Geochimica et Cosmochimica Acta, 74, 784-798.

946   Matzen, A.K., Baker, M.B., Becker, J.R., Wood, B.J., and Stolper, E.M. (2017) The effect of liquid composition
947   on the partitioning of Ni between olivine and Site melt. Contributions to Mineralogy and Petrology,
948   172:3, doi. 10.1007/s00410-016-1319-8.

949   Meschede, M. (1986) A method of discriminating between different types of mid-ocean ridge basalts and
950   continental tholeiites with the Nb-Zr-Y diagram. Chemical Geology 56, 207-218.

951   Metcalf, R.V. and Shervais, J.W. (2008) Suprasubduction-zone ophiolites: Is there really an ophiolite
952   conundrum? The Geological Society of America Special Paper, 408, 191-222, doi: 0.1130/2008.2438(07).

953   Meijer, A., Reagan, M., Ellis, H., Shafiqullah, M., Sutter, J., Damon, P., Kling, S. (1983) Chronology of volcanic
954   events in the eastern Philippine Sea. In: Hayes, D.E. (Ed.), The tectonic and geologic evolution of
955   southeast Asian seas and islands: Part. Geophysical Monograph, vol. 27, pp. 349-359.

40

956   McDonough, W.F. and Sun, S.S. (1995) The composition of the Earth. Chemical Geology 120, 223–253.

957   Mitchell, A.L. and Grove, T.L. (2015) Melting the hydrous, subarc mantle: The origin of primitive andesites;

958   Contributions to Mineralogy and Petrology, 170:13, doi: 10.1007/s00410-015-1161-4.

959   Miyashiro, A. (1973) The Troodos ophiolitic complex was probably formed in an island arc. Earth and Planetary

960   Science Letters, 19, 218-224.

961   Moghadam, H.S., and Stern, R.J. (2014) Ophiolites of Iran: Keys to understanding the tectonic evolution of SW

962   Asia: (I) Paleozoic ophiolites. Gondwana Research, 91, 19-38.

963   Moghadam, H.S., Zaki Khedr, M., Chiaradia, M., Stern, R.J., Bakhshizad, F., Arai, S., Ottley, C.J., and Akihiro,

964   T. (2014) Supra-subduction zone magmatism of the Neyriz ophiolite, Iran: Constraints from geochemistry

965   and Sr-Nd-Pb isotopes. International Geology Review 56(11), 1395-1412.

966   Monnier, C., Girardeau, J., Maury, R.C., Cotten, J. (1995) Back-arc basin origin for the East Sulawesi ophiolite

967   (eastern Indonesia). Geology, 23, 851-854.

968   Moores, E.M. (1982) Origin and emplacement of ophiolites. Reviews of Geophysics and Space Physics, 20, 735-

969   760.

970   Murata, K.J. and Richter, D.H. (1966) Chemistry of the lavas of the 1959-60 eruption of Kilauea Volcano,

971   Hawaii. United States Geological Survey, Professional Paper P 0537-A: A1-A26.

972   Murton B.J. (1989) Tectonic controls on boninite genesis. In: A.D. Saunders and M.J. Norry (Eds.), Magmatism

973   in the Ocean Basins. Geol. Soc. London Spec. Publ., 42: 347-377.

974   Neave, D. and Putirka, K. (2017) A new clinopyroxene-liquid barometer, and implications for magma storage

975   pressures under Icelandic rift zones. American Mineralogist, 102, in press.

976   Niles, X., Nelson, W., Reagan, M.K., Pearce, J.A., Chapman, T., Godard, M., Heaton, D.E., Kirchenbauer, M.,

977   Li, H., Prytulak, J., Ryan, J.G., Shervais, J.W., Shimizu K., Whattam, S.A., and Expedition 352 Science

978   Party (2016) $^{187}Os/^{188}Os$ of boninites from the Izu-Bonin Mariana forearc, IODP Exp. 352. AGU Fall

979   Meeting 2016.

980   Niu, Y., O'Hara, M.J., and Pearce, J. (2003) Initiation of subduction zones as a consequence of lateral

981   compositional buoyancy contrast within the lithosphere: A petrological perspective. Journal of Petrology,

982   44, 851–866. http://dx.doi.org/10.1093/petrology/44.5.851.

REVISION 5

983   Ochs, F.A. III, and Lange, R.A. (1999) The density of hydrous magmatic liquids. Science, 283,1314-1317. doi:

984   10.1126/science.283.5406.1314.

985   Parkinson, I.J., and Pearce, J.A. (1998) Peridotites from the Izu-Bonin-Mariana forearc (ODP Leg 125):

986   Evidence for mantle melting and melt-mantle interaction in a supra-subduction zone setting. Journal of

987   Petrology, 39, 1577-1618.

988   Pearce J.A. (1982) Trace element characteristics of lavas from destructive plate boundaries. In: R.S. Thorpe

989   (Ed.), Andesites. John Wiley & Sons, New York, p. 525-548.

990   Pearce, J.A. (2003) Supra-subduction zone ophiolites: The search for modern analogues. In: Dilek, Y.,

991   Newcomb, S. (Eds.), Ophiolite concept and the evolution of geological thought. Geological Society of

992   America Special Paper 373, pp. 269–293.

993   Pearce, J.A. (2008) Geochemical fingerprinting of oceanic basalts with applications to ophiolite classification

994   and the search for Archean oceanic crust. Lithos, 100, 14-48.

995   Pearce, J.A., Barker, P.F., Edwards, S.J., Parkinson, I.J., and Leat, P.T. (2000) Geochemistry and tectonic

996   significance of peridotites from the South Sandwich arc-basin system, South Atlantic. Contributions to

997   Mineralogy and Petrology 139, 36-53.

998   Pearce, J.A., Harris, N.B.W., and Tindle, A.G. (1984) Trace element discrimination diagrams for the tectonic

999   interpretation of granitic rocks. Journal of Petrology 25, 956-983.

1000   Pearce, J.A., Kempton, P.D., Nowell, G.M., and Noble, S.R. (1999) Hf-Nd element and isotope perspective on

1001   the nature and provenance of mantle and subduction components in western   Pacific   arc-basin

1002   systems. Journal of Petrology, 40, 1579–1611, http://dx.doi.org/10.1093/petroj/40.11.1579.

1003   Pearce, J.A., Lann, S.R., Arculus, R.J., Murton, B.J., Ishii, T., Peate, D.W., and Parkinson, I.J. (1992) Boninite

1004   and harzburgite from Leg 125 (Bonin-Mariana fore-arc): A case study of magma genesis during the initial

1005   stages of subduction. In: Fryer, P., Peace, J. A. & Stokking, L. B. (eds) *Proceedings of the Ocean Drilling

1006   Program, Scientific Results, 125*. College Station, TX: Ocean Drilling Program, pp. 623-659.

1007   Pearce, J.A., Lippard, S.J., and Roberts, S. (1984) Characteristics and tectonic significance of supra-subduction

1008   zone ophiolites. In: Kokelaar, P., Howells, M. (Eds.), Geology of marginal basins. Geological Society of

1009   London Special Publication 16, pp 77–94.

1010   Pearce, J.A. and Norry, N.J. (1979) Petrogenetic implications of Ti, Zr, Y, and Nb variations in volcanic rocks.

1011   Contributions to Mineralogy and Petrology, 69, 33-49.

1012   Pearce, J.A. and Reagan, M.K. (2019) Identification, classification, and interpretation of boninites from

1013   Anthropocene   to   Eoarchean   using   Si-Mg-Ti   systematics.   Geosphere,   15,

1014   https://doi.org/10.1130/GES01661.1

1015   Pearce, J.A., and Robinson, P.T. (2010) The Troodos ophiolitic complex probably formed in a subduction

1016   initation, slab edge setting. Gondwana Research, 18(1), 60-81. doi:10.1016/j.gr.2009.12.003.

1017   Portnyagin, M.V., Danyushevsky, L.V., Kamenetsky, V.S. (1997) Coexistence of two distinct mantle sources

1018   during formation of ophiolites: A case study of primitive pilliow-lavas from the lowest part of the

1019   volcanic section of the Troodos Ophiolite, Cyprus. Contributions to Mineralogy and Petrology, 128, 287-

1020   301.

1021   Putirka, K.D. (2008) Thermometers and barometers for volcanic systems. In: Putirka, K.D., Tepley, F. (Eds.),

1022   Reviews of Mineralogy and Geochemistry, 69, 61-120.

1023   Putirka, K., Johnson, M., Kinzler, R., and Walker D. (1996) Thermobarometry of mafic igneous rocks based on

1024   clinopyroxene-liquid equilibria, 0-30 kbar. Contributions to Mineralogy and Petrology, 123, 92-108.

1025   Putirka, K.D., Perfit, M., Ryerson, F.J., and Jackson, M.G. (2007), Ambient and excess mantle temperatures,

1026   olivine thermometry, and active vs. passive upwelling. Chemical Geology, 241, 177-206.

1027   http://dx.doi.org/10.1016/j.chemgeo.2007.01.014.

1028   Putirka, K., Ryerson, F. J., Mikaelian, H. and (2003) New igneous thermobarometers for mafic and evolved lava

1029   compositions, based on clinopyroxene + liquid equilibria. American Mineralogist, 88, 1542-1554.

1030   Putirka, K.D., Ryerson, F. J., Perfit, M., and Ridley, W.I. (2011) Mineralogy and composition of oceanic mantle.

1031   Journal of Petrology, 52, 279-313.

1032   Reagan, M.K., Heaton, D.E., Schmizt, M.D., Pearce, J.A., Shervais, J.W. and Koppers, A.P, 2019. Forearc ages

1033   reveal extensive short-lived and rapid seafloor spreading following subduction initiation. Earth and

1034   Planetary Science Letters 506, 520-529. https://doi.org/10.1016/j.epsl.2018.11.020.

1035   Reagan, M.K., Ishizuka, O., Stern, R.J., Kelley, K.A., Ohara, Y., Blichert-Toft J., Bloomer, S.H., Cash, J.,

1036   Fryer, P., Hanan, B.B., Hickey-Vargas, R., Ishii, T., Kimura, J.I., Peate, D.W., Rowe, M.C., Woods, M.

1037   (2010) Fore-arc basalts and subduction initiation in the Izu-Bonin-Mariana system.   Geochemistry,

43

1038   Geophysics, Geosystems 11, Q03X12, doi:10.1029/2009GC002871.

1039 Reagan, M.K., McClelland, W.C., Girard, G., Goff, K.R., Peate, D.W., Ohara, Y., and Stern, R.J. (2013) The

1040   geology of the southern Mariana fore-arc crust: implications for the scale of Eocene volcanism in the

1041   western Pacific. Earth and Planetary Science Letters, 380, 41-1.,

1042   http://dx.doi.org/10.1016/j.epsl.2013.08.013.

1043 Reagan, M.K., Pearce, J.A., Petronotis, K., and the Expedition 352 Scientists (2015) Izu-Bonin-Mariana Fore

1044   Arc. Proceedings of the International Ocean Discovery Program, 352: College Station, TX (*International*

1045   *Ocean Discovery Program*), http://dx.doi.org/10.14379/iodp.proc.352.2015.

1046 Reagan, M.K., Pearce, J.A., Petronotis, K., Almeev, R.R., Avery, A.J., Carvallo, C., Chapman, T., Christeson,

1047   G.L., Ferré, E.C., Godard, M., Heaton, D.E., Kirchenbaur, M., Kurz, W., Kutterolf, S., Li, H., Li, Y.,

1048   Mishibayashi, K., Morgan, S., Nelson, W.R., Prytulak, J., Python, M., Robertson, A.H.F., Ryan, J.G.,

1049   Sager, W.W., Sakuyama, T., Shervais, J.W., Shimizu, K., and Whattam, S.A. (2017) Subduction

1050   initiation and ophiolite crust: New insights from IODP drilling. International Geology Review,

1051   http://dx.doi.org/10.1080/00206814.2016.1276482.

1052 Reay, A., Johnstone, R.A., and Kawachi, Y. (1989) Kaersutite, a possible international microprobe standard.

1053   Geostandard Newsletter, 13, 187-190.

1054 Rhodes, J.M., Lofgren, G.E., and Smith, B.P. (1979) One atmosphere melting experiments on ilmenite basalt 12

1055   000. Proceedings of the 10th Lunar Science Conference, pp. 407-422.

1056 Rioux, M., Bowring, S., Kelemen, P., Gordon, S., Dudás, F., and Miller, R. (2012) Rapid crustal accretion and

1057   magma assimilation in the Oman-U.A.E. ophiolite: High precision U-Pb zircon geochronology of the

1058   gabbroic crust, doi:10.1029/2012JB009273.

1059 Rollinson, H.R. (2003). *Using Geochemical Data: Evaluation, Presentation, Interpretation* (Longman

1060   Geochemistry Series), 352 pp.

1061 Saccani, E. and Photiades, A. (2004) Mid-ocean ridge and supra-subduction affinities in the Pindos Massif

1062   ophiolites (Greece): Implications for magma genesis in a proto-forearc setting, Lithos 73, 229–253.

1063 Saccani, E., Bortolotti, V., Marroni, M., Pandolfi, L., Photiades, A., and Principi, G. (2008) The Jurassic

1064   association of backarc basin ophiolites and calk-alkaline volcanics in the Guevgueli Complex (northern

1065   Greece): Implication for the evolution of the Vardar Zone, Ophioliti, 33, 209-227.

1066   Sato, H. (1977) Nickel content of basaltic magmas: Identification of primary magmas and a measure of the

1067   degree of olivine fractionation, Lithos, 10, 113-120.

1068   Scruggs, M.A. and Putirka, K.D. (2018) Eruption triggering by partial crystallization of mafic enclaves at Chaos

1069   Crags, Lassen Volcanic Center, California, American Mineralogist, 103, 1575-1590,

1070   https://doi.org/10.2138/am-2018-6058.

1071   Shervais, J.W. (1982) Ti-V plots and the petrogenesis of modern and ophiolitic lavas, Earth and Planetary

1072   Science Letters, 59, 110-118.

1073   Shervais, J.W. (2001) Birth, death and resurrection: The life cycle of supra-subduction zone ophiolites,

1074   Geochemistry, Geophysics, Geosystems, 2, Paper 2000GC000080.

1075   Shervais, J.W. et al. (2017) Chemostratigraphy of subduction initiation: Boninite and forearc basalt from IODP

1076   Expedition 352. EGU General Assembly.

1077   Shervais, J.W., Reagan, M., Haugen, E., Almeev, R., Pearce, J., Prytulak, J., Ryan, J.G., Whattam, S.A., Godard,

1078   M., Chapman, T., Li, H., Kurz, W., Nelson, W.R., Heaton, D., Kirchenbaur, M., Shimizu, K., Sakuyama,

1079   T., Li, Y., and Vetter, S.K. (2019) Magmatic response to subduction initiation, Part I: Fore-arc basalts of

1080   the Izu-Bonin Arc from IODP Expedition 352. Geochemistry, Geophysics, Geosystems, *20/1, 314-338,*

1081   *Article GGGE21778,* DOI:10.1029/2018GC007731.

1082   Sobolev, A.V. and Danyushevsky, L.V. (1994) Petrology and geochemistry of boninites from the north

1083   termination of the Tonga Trench: Constrains on the generation conditions of primary high-Ca boninite

1084   magmas, Journal of Petrology, 35, 1183-1211.

1085   Sobolev, A.V., Portnyagin, M.V., Dmitriev, L.V., Tsameryan, O.P., Danyushevsky, L.V., Kononkova, N.N.,

1086   Schimizu, N., Robinson, P.T.(1993). Petrology of ultramafic lavas and associated rocks of the Troodos

1087   Massif, Cyprus. Petrology 1, 331–361.

1088   Spera, F.J. (1980) Aspects of magma transport in R.B. Hargraves (ed.) *Physics of Magmatic Processes*,

1089   Princeton University Press, 265-324.

1090   Spera, F.J. (1984) Carbon dioxide in petrogenesis III: Role of volatiles in ascent of alkaline magmas with special

1091   reference to xenolith-bearing lavas, Contributions to Mineralogy and Petrology 88, 217-232.

1092   Stern, R.J., Bloomer, S.H. (1992) Subduction zone infancy: Examples from the Eocene Izu-Bonin-Mariana and

1093   Jurassic California, Geological Society of America Bulletin, 104, 1621-1636.

1094   Stern, R.J. (2004) Subduction initiation: spontaneous and induced. Earth and Planetary Science Letters, 226,

1095   275–292. http://dx.doi.org/10.1016/j.epsl.2004.08.007.

1096   Stern, R.J., Reagan, M., Ishizuka, O., Ohara, Y. and Whattam, S. (2012), To Understand Subduction Initiation,

1097   Study Forearc Crust; To Understand Forearc Crust, Study Ophiolites, Lithosphere, 4, 469-483.

1098   Straub, S.M., LaGatta, A.B., Lilian Martin-Del Pozzo, A., and Langmuir, C.H. (2008) Evidence from high-Ni

1099   olivines for a hybridized peridotite/pyroxenite source for orogenic andesites from the central Mexican

1100   Volcanic Belt. Geochemistry, Geophysics, Geosystems, 9, doi.10.1029/2007GC001583.

1101   Straub S. M., Gómez-Tuena, A., Stuart, F. M., Zellmer, G. F., Espinasa-Perena, R., Cai, M. Y., Iizuka, Y.,

1102   (2011) Formation of hybrid arc andesites beneath thick continental crust. Earth and Planetary Science

1103   Letters, 303, 337–347

1104   Takahashi, E., Uto, K., and Schilling, J.G. (1987) Primary magma compositions and Mg/Fe ratios of the mantle

1105   residues along Mid Atlantic Ridge 29°N to 73°N, Technical reports of ISEI, Okayama University, A9, pp.

1106   1-14.

1107   Tanaka, H.K.M., Kusagaya, T., and Shinohara, H. (2014) Radiographic visualization of magma dynamics in an

1108   erupting volcano. Nature Communications, 5:3381. doi: 10.1038/ncomms4381.

1109   Tatsumi, Y. (1981) Melting experiments on a high-Mg andesite, Earth and Planetary Science Letters, 54, 357-

1110   365.

1111   Tatsumi, Y. (1982) Origin of high-Mg andesites in the Setouchi volcanic belt, southwest Japan, II. Melting phase

1112   relations at high pressures, Earth and Planetary Science Letters, 60, 305-317.

1113   Tatsumi, Y., and Maruyama, S. (1989) Boninites and high-Mg andesites: Tectonics and petrogenesis. In,

1114   Crawford, A.J. (Ed.), *Boninites and related rocks*. London: Unwin and Hyman, pp. 50-71.

1115   Taylor, R.N., Nesbitt, R.W., Vidal, P., Harmon, R.S., Auvray, B., and Croudace, I.W. (1994) Mineralogy,

1116   chemistry, and genesis of the boninite series volcanics, Chichijima, Bonin Islands, Japan, Journal of

1117   Petrology, 35(3), 577-617.

1118   Thompson, G.M., Malpas, J., and Smith, I.E.M. (1997) The geochemistry of tholeiitic and alkalic plutonic rocks

1119   within the Northland ophiolite, northern New Zealand: Magmatism in a back arc basin, Chemical

1120   Geology, 142, 213-223.

REVISION 5

1121   Topliss, M.J., and Carroll, M.R. (1995) An experimental study of the influence of oxygen fugacity on Fe-Ti

1122   oxide stability, phase relations and mineral-melt equilibria in ferro-basaltic systems, Journal of Petrology,

1123   36, 1137-1170.

1124   Torró, L., Proenza, J.A., Marchesi, C., Garcia-Casco, A., and Lewis, J.F. (2017) Petrogenesis of meta-volcanic

1125   rocks from the Maimón Formation (Dominican Republic): Geochemical record of the nascent Greater

1126   Antilles paleo-arc, Lithos, 278-281, 255-273, http://dx.doi.org/10.1016/j.lithos.2017.01.031.

1127   Umino, S. (1986) Magma mixing in boninite sequence of Chichijima, Bonin Islands, Journal of Volcanology and

1128   Geothermal Research, 29, 125-157.

1129   Umino, S., and Kushiro, I. (1989) Experimental studies on boninite petrogenesis. In: Crawford, A. J. (ed.)

1130   *Boninite and Related Rocks*. London: Unwin Hyman, pp. 89-109.

1131   van der Laan, S.R., Arculus, R.J., Pearce, J.A., and Murton, B.J. (1992) Petrography, mineral chemistry, and

1132   phase relations of the basement boninite series of Site 786, Izu-Bonin forearc. In: Fryer, P., Pearce, J.A.,

1133   et al. (Eds.), *Proceedings of the Ocean Drilling Program, Scientific results, Volume 125*: College Station,

1134   Texas, Ocean Drilling Program, p. 171-201.

1135   van der Laan, S.R., Flower, M.F.J., Koster Van Groos, A.K. (1989) Experimental evidence for the origin of

1136   boninites: near-liquidus phase relations to 7.5 kbar. In: Crawford, A. J. (ed.) *Boninite and Related Rocks*.

1137   London: Unwin Hyman, pp. 112^-47.

1138   Venezsky, D.Y., and Rutherford, M.J. (1999) Petrology and Fe-Ti oxide reequilibration of the 1991 Mount

1139   Unzen mixed magma, Journal of Volcanology and Geothermal Research, 89, 213-230.

1140   Walker, D.A. and Cameron, W.E. (1983) Boninite primary magmas: Evidence from the Cape Vogel peninsula,

1141   PNG, Contributions to Mineralogy and Petrology, 83, 150-158.

1142   Wang, Z., and Gaetani, G.A. (2008) Partitioning of Ni between olivine and siliceous eclogite partial melt:

1143   experimental constraints on the mantle source of Hawaiian basalts, Contributions to Mineralogy and

1144   Petrology, 156, 661-678.

1145   Whattam, S.A. (2009) Arc-continent collisional orogenesis in the SW Pacific and the nature, source and

1146   correlation of emplaced ophiolitic nappe components, Lithos, 113, 88-114.

1147   Whattam, S.A. (2018) Primitive magmas in the early Central American Arc system generated by plume-induced

1148   subduction initiation, Frontiers in Earth Science, 6:114. doi: 10.3389/feart.2018.00114.

1149   Whattam, S.A. Montes, C. and Stern, R.J. (2020) Early Central American forearc follows the subduction

1150   initiation rule, Gondwana Research, https://doi.org/10.1016/j.gr.2019.10.002.

1151   Whattam, S.A., and Stern, R.J. (2011) The 'subduction initation rule': A key for linking ophiolites, intra-oceanic

1152   arcs and subduction initiation, Contributions to Mineralogy and Petrology, 162, 1031-1045, doi:

1153   10.1007/s00410-011-0638-z.

1154   Witt-Eickschen, G. and Seck, H.A. (1991) Solubility of Ca and Al in orthopyroxene from spinel peridotite: An

1155   improved version of an empirical geothermometer, Contributions to Mineralogy and Petrology, 106, 431-

1156   439.

1157   Wood, D.A. (1980) The application of Th-Hf-Ta diagram to problems of tectonomagmatic classification and to

1158   establishing the nature of crustal contamination of basaltic lavas of the British Tertiary volcanic province,

1159   Earth and Planetary Science Letters, 42, 77-97.

1160   Wu, J., Suppe, J., and Kanda, R. (2016) Philippine Sea and East Asian plate tectonics since 52 Ma constrained

1161   by new subducted slab reconstruction methods. Journal of Geophysical Research, 121, 4670–4741,

1162   doi:10.1002/2016JB012923.

1163   Yajima, K., and Fujimaki, H. (2001) High-Ca and low-Ca boninites from Chichijima, Bonin (Ogasawara)

1164   archipelago, Japanese Magazine of Mineralogical and Petrological Sciences, 30, 217-236.

1165   Yogodzinski, G. M., Bizimis, M., Hickey-Vargas, R., McCarthy, A., Hocking, B. D., Savov, I. P., et al. (2018).

1166   Implications of Eocene-age Philippine Sea and forearc basalts for initiation and early history of the Izu-

1167   Bonin-Mariana   arc.   Geochimica   et   Cosmochimica   Acta,   228,   136–156.

1168   https://doi.org/10.1016/j.gca.2018.02.047

1169   Zhou, J.-H., and Asimow, P.D. (2014) Neoproterozoic boninite-series rocks in South China: A depleted source

1170   modified by sediment-derived melt, Chemical Geology, 388, 98-111.

1171

1172

1173

Table 1 Modal estimates of forearc basalts and boninites

Phase	FAB (n = 17)		TS 93 AND (n = 1)	HMA (n = 5)		BB (n = 8)		LSB (n = 14)		HSB (n = 13)	
Phenocrysts	Mean %	Range %		Mean %	Range %	Mean %	Range %	Mean %	Range %	Mean %	Range %
Olivine	-	-	-	0.6	0 - 3	6	1 – 14	8.9	0 -30	2	0 - 10
Orthopyroxene	-	-	-	0.3	0 - 1	4	2 – 8	0.4	0 - 2	4.5	0 - 15
Clinopyroxene	1.2	0.3-2.0	2	2.3	0 - 15	3	1 – 5	1.1	0 - 6	0.1	0 - 0.5
Plagioclase	1.5	0.2-5	1	1.3	0-5	-	-	-	-	-	-
Magnetite	-	-	-	-	-	-	-	-	-	-	-
Chromite	-	-	-	-	-	0.7	0.5-1	0.8	0 - 1	0.01	0 - 0.1
Groundmass	Mean %	Range %		Mean %	Range %			Mean %	Range %	Mean %	Range %
Orthopyroxene	-	-	-	1.6	0 - 10	15	10 –20	1	0 - 10	21	0 - 55
Clinopyroxene	20	8.0-35	-	15	8.0 - 25	22.5	10– 35	20	0 - 65	18	0 - 60
Plagioclase	38	10.0- 53	37	38	25 - 55	50	50	14	0 - 50	-	-
Magnetite	2	1.0 -3.0	-	1	0 - 3			-	-	-	-
Chromite	-	-	-	-	-			0	0 - 1	-	-
Glass (original %)	5.6	0 - 82	-	*	-	40	30 –50	22	0 –100	46	0 - 100
Mesostasis[1]	15	0 - 48	54	42	19 - 59	45	16 –79	32	0 –70	33	0 - 65
Vesicles	1.6	0 - 15	3	7	0 - 20	11	3 –20	11	1.0 - 40	6	0 - 15

Abbreviations: FAB, forearc basalt; AND, andesite; HMA, high-Mg-andesite; BB, basaltic boninite; LSB low-Si boninite; HSB high-Si boninite

Phenocrysts include microphenocrysts; chromite typically occurs as inclusions in olivine.

[1] Mesostasis here refers to microlites and cryptocrystalline quench phases. Includes devitrified glass.

* One HMA has 73% glass; all of the others have 0%. Note that TS 93 is an anomalous andesite (see text).

Whattam et al. 2020

Table 2 Summary of petrographic features of forearc basalts, boninites and high magnesium andesites

Rock type	Phenocrysts	Microlites	Groundmass	Alteration	Textural features
FAB	PL: 0.1-1.5 mm	PL	Altered (oxidized)	Oxidation of crypto-	Predominantly equigranular,
	CPX: 0.2-1.2 mm	CPX (rare)	to unidentifiable	crystalline	intersertal and intergranular;
			secondary products; glass	groundmass, veinlets	minor subophitic relations
			commonly devitrified	of carbonates	
TS 93 AND	PL: 0.4 mm	PL	PL altered to zeolites in part,	zeolites, chlorite	Intersertal groundmass
	CPX: 0.6 mm	CPX	CPX altered to chlorite in part.		with augite phenocrysts
			Mesostasis completely altered to		
			unidentified secondary products		
HMA	PL: 0.3-0.4 mm	-	Equigranular plagioclase	Groundmass	Equigranular and intergranular, the latter
	PX: <0.5 mm		set in cryptocrystalline	plagioclase laths and	of which is defined by the occupation of
			groundmass	cryptocrystalline	pyroxenes in the interstices of randomly
				materials	oriented plagioclase laths
				ubiquitously altered/	
				oxidized	
BB	OL: 0.4-7 mm	PL: 0.3	Glass or fine-grained mesostasis	Olivine phenocrysts	Phyric, hyalopilitic, OPX ML rimmed by CPX,
	OPX: 0.8-5	OPX: 0.2	Typically altered to clay, zeolites	occasionally replaced	OL mantled by OPX, rare glomerocrysts
	CPX: 0.2-5	CPX: 0.2	and carbonate.	by clay, discrete zeolites	of OPX, rare oscillatory zonation of OPX,
	CHR: 0.2-1				vesicles rare
LSB	OL: 0.3-3.0 mm	OPX	Predominantly hyalopilitic	Minor carbonates	Phyric, hyalopilitic, OPX ML rimmed by CPX,
	OPX: 0.2-0.8 mm	CPX	with clear fresh glass	and zeolites	OL mantled by OPX, rare glomerocrysts
	CPX: 0.3-0.5 mm		moderately altered	in veinlets	of OPX, rare oscillatory zonation of OPX,
	CHR: 0.2 mm		glass rare		vesicles rare
HSB	OL: 0.1-1.6 mm		Predominantly hyalopilitic	Oxidation and	Phyric, OPX ML rimmed by CPX,
	OPX: 0.15-1.5 mm	OPX	with clear fresh glass;	palagonitization of	glomerocrysts of OPX common,
	CPX: ≤0.2 mm	CPX[1]	moderately altered	glass, veinlets of	vesicularity up to 15%, devitrification
			glass rare	carbonates and glass	spherules common

Abbreviations: FAB, forearc basalt; AND, andesite; HMA, high-Mg-andesite; BB, basaltic boninite; LSB low-Si boninite; HSB high-Si boninite

Note that TS 93 is an anomalous andesite (see text).

Whattam et al. 2020

Table 3 Thermobarometry summary						
Rock Type	Thermobarometer	*n*	P, μ (kbar)	P, range (kbar)	T, μ (°C)	T, range (°C)
FAB	clinopyroxene	11	**2.4 ± 0.4**	0.5-4.6	**1163 ± 14**	1142-1190
HMA	orthopyroxene	1	**0.2 ± 0.05**	-	**1193 ± 26**	-
LSB	orthopyroxene	1	**0.3 ± 0.1**	-	**1214 ± 9**	-
HSB	orthopyroxene	6	**0.3 ± 0.1**	0.2-0.4	**1249 ± 13**	1235-1264
LSB	olivine	14	**-**	-	**1172 ± 23**	1119-1202
HSB	olivine	8	**-**	-	**1152 ± 24**	1125-1190
PetDB MORB	clinopyroxene	75	**1.4 ± 0.2**	-1.8-8.3	**1182 ± 15**	1133-1240

Refer to Supplementary Tables 10-12 for specific thermobarometers employed. Uncertainties associated with estimated P and T are ± 1 kbar and ± 30°C, respectively. Means are in bold and uncertainty assigned to the mean is the standard deviation.

Whattam et al. 2020
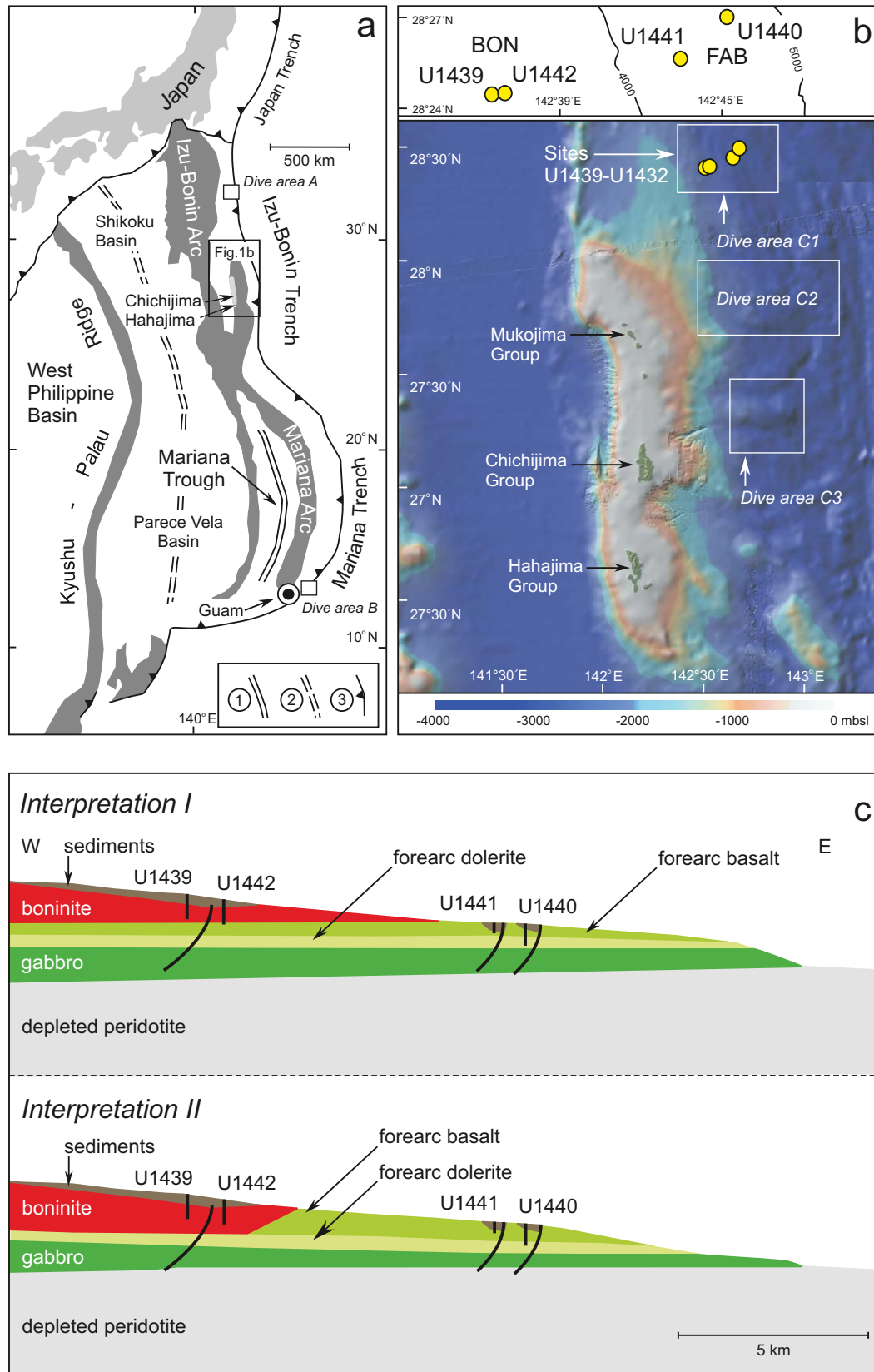
Figure 1 Whattam et al., 2018
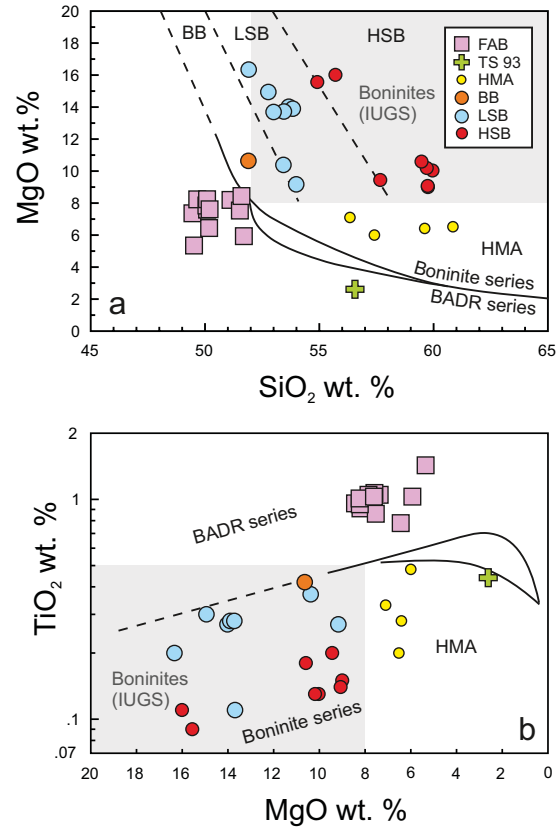
Figure 2 Whattam et al. 2018
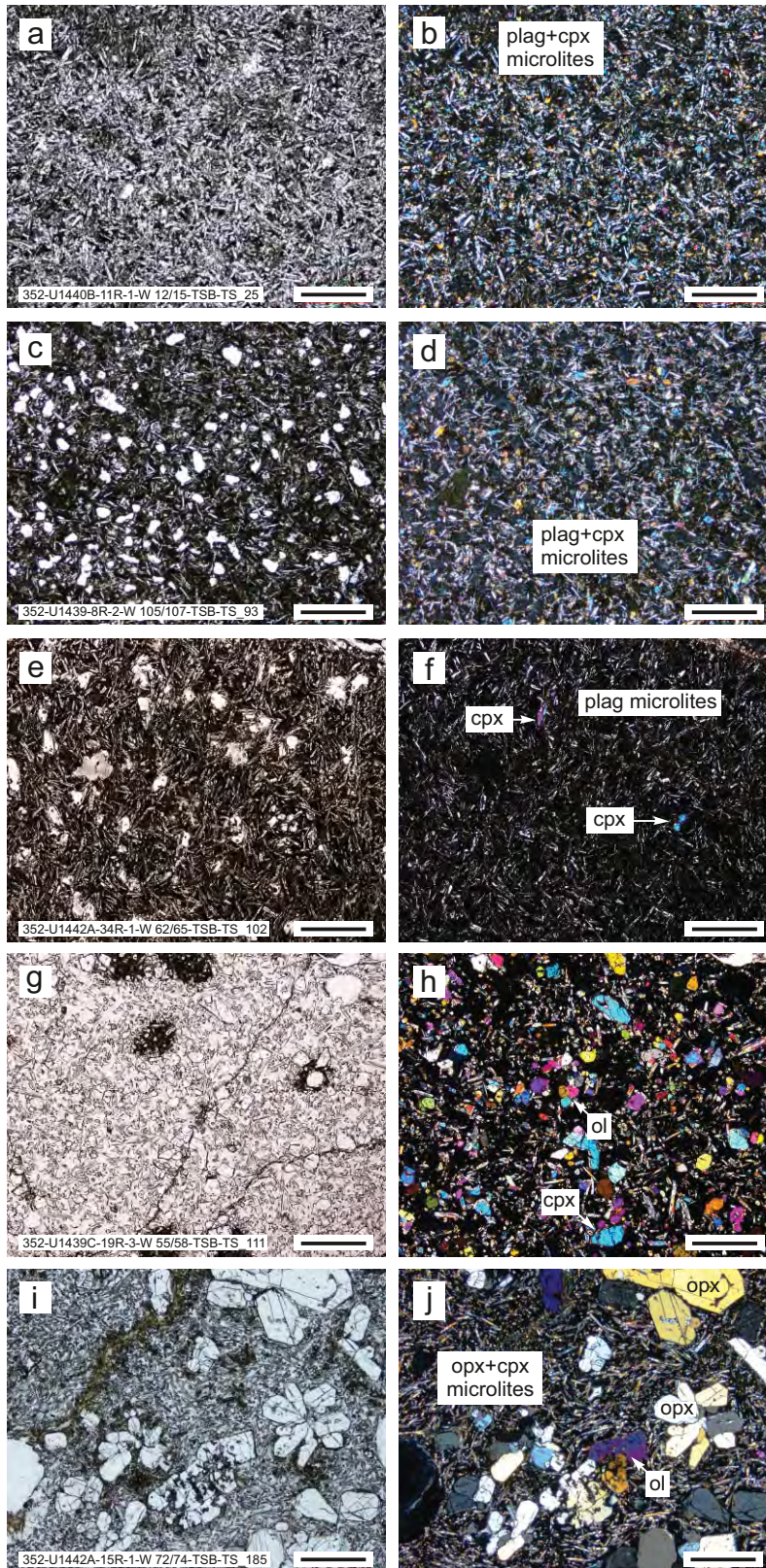
Figure 3 Whattam et al. 2018
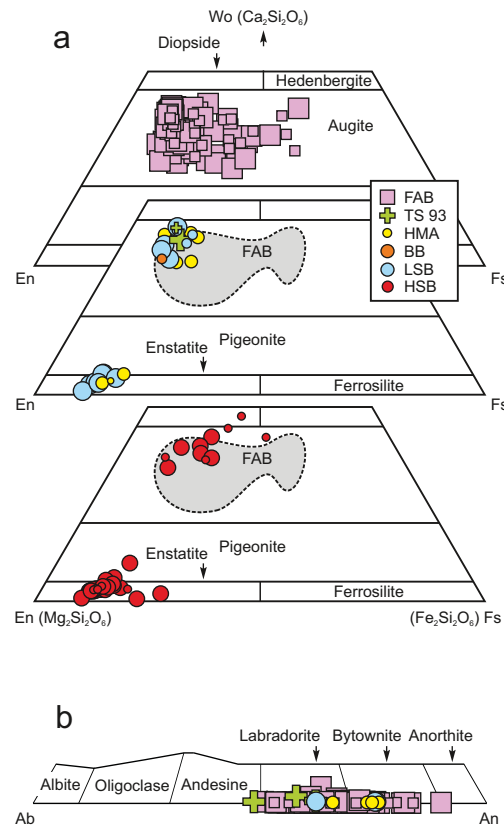
Figure 4 Whattam et al. 2018
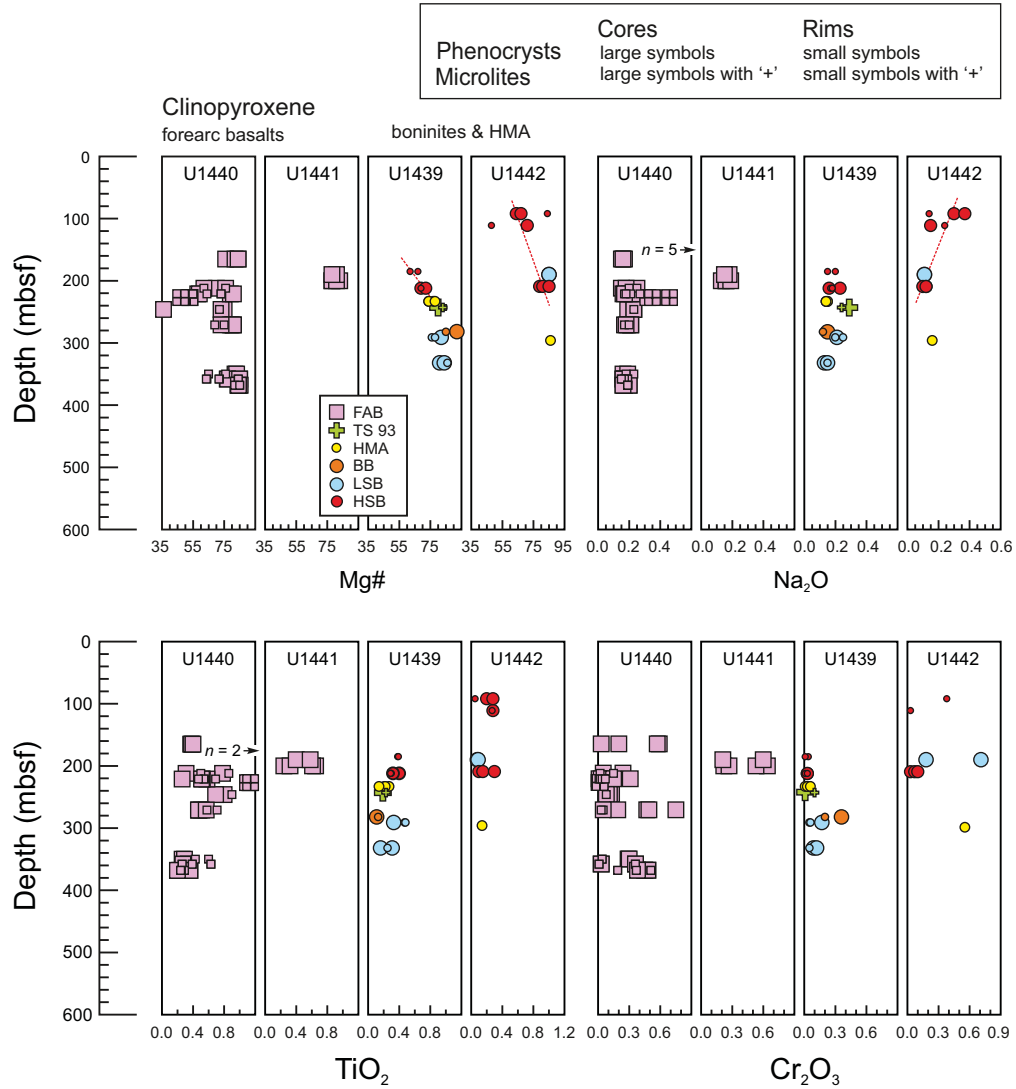
Figure 5 Whattam et al. 2018
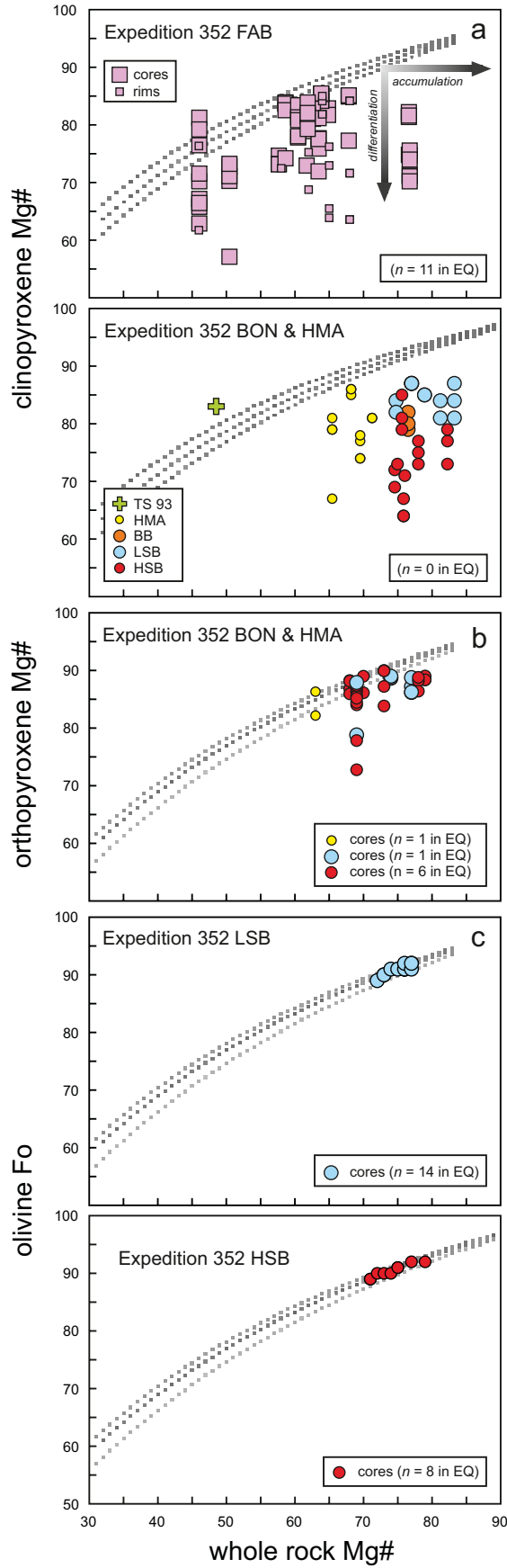
Figure 6 Whattam et al. 2019
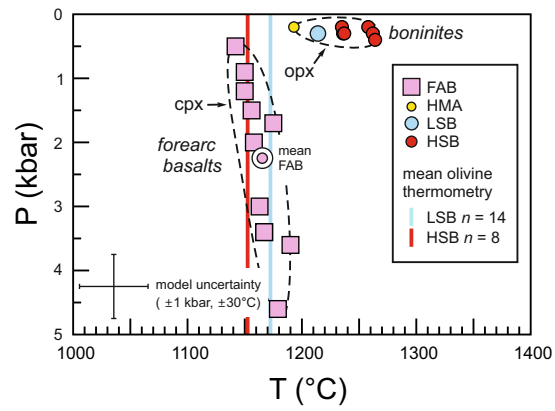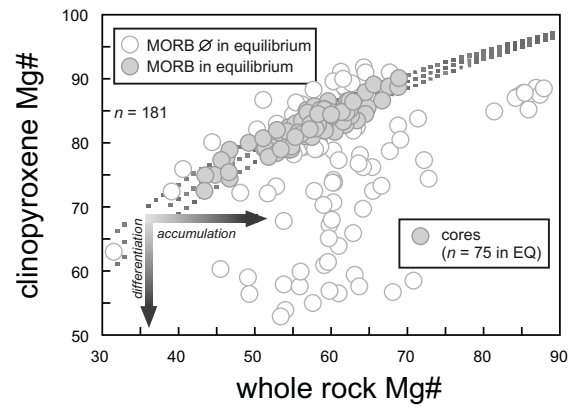
Figure 7 Whattam et al. 2019
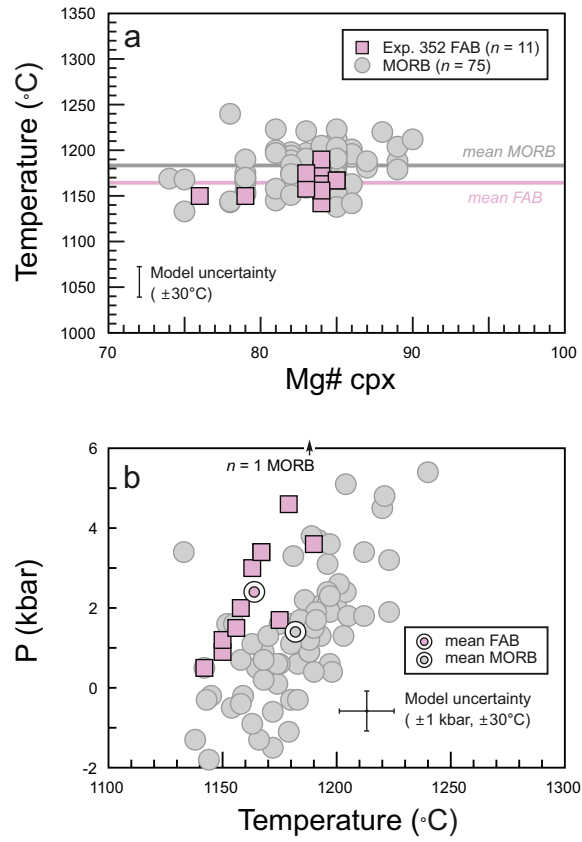
Figure 8 Whattam et al. 2019
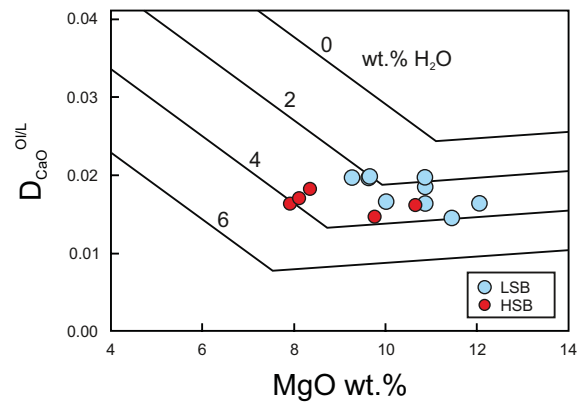
Figure 9 Whattam et al. 2019
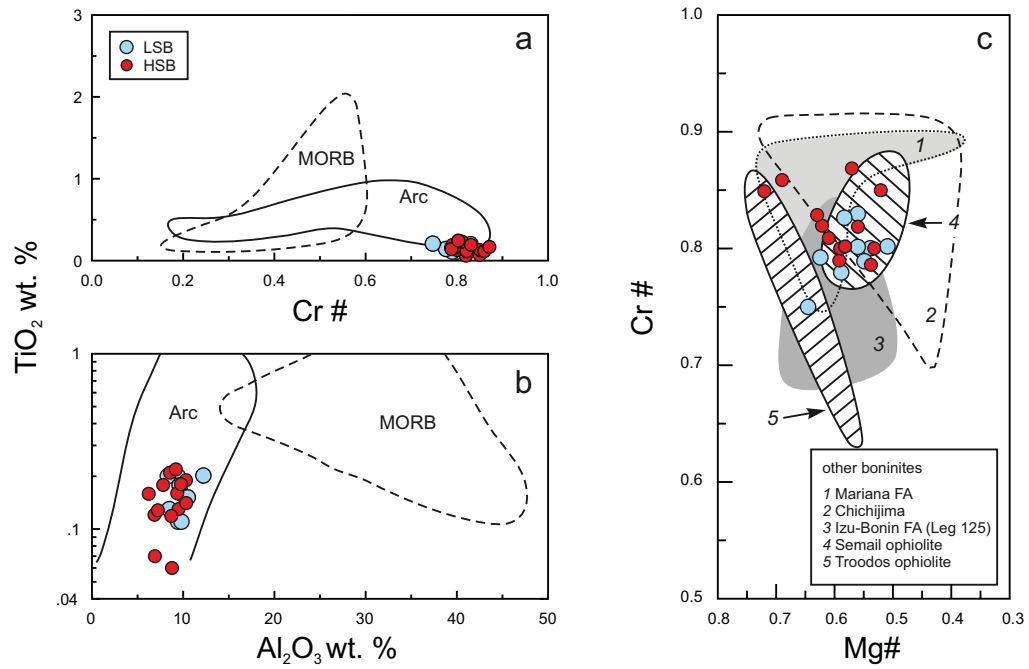
Figure 10 Whattam et al. 2019
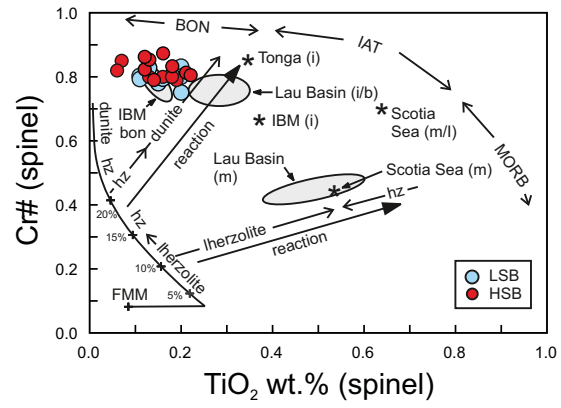
Figure 11 Whattam et al. 2019
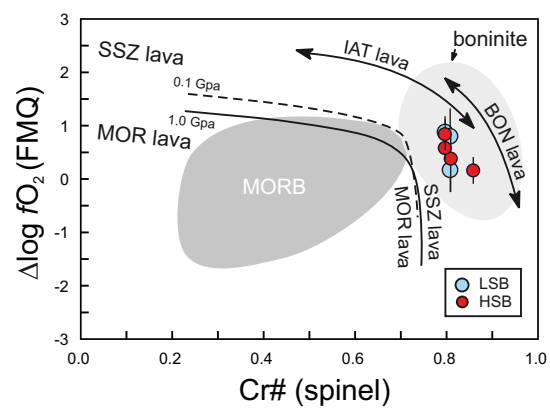
Figure 12 Whattam et al. 2019
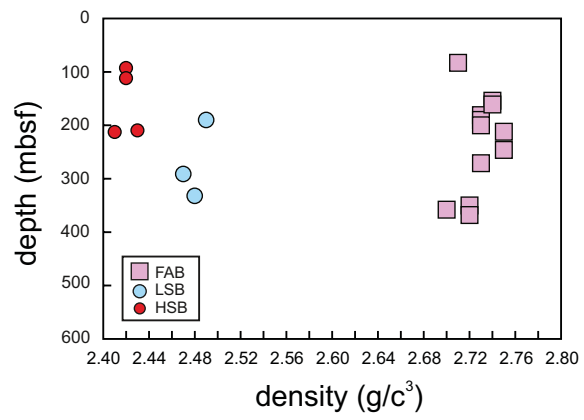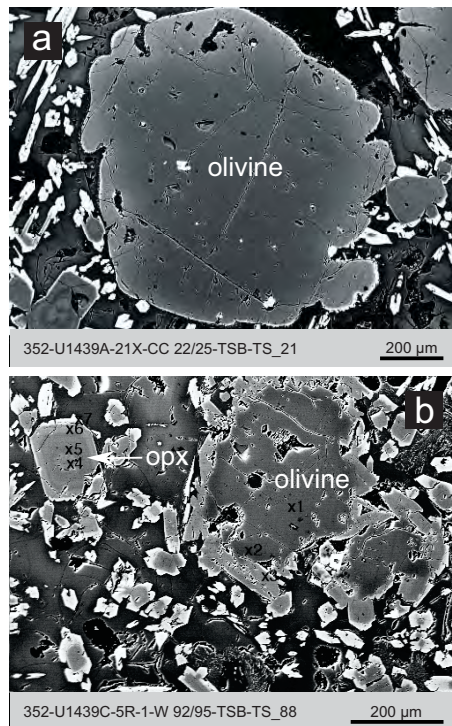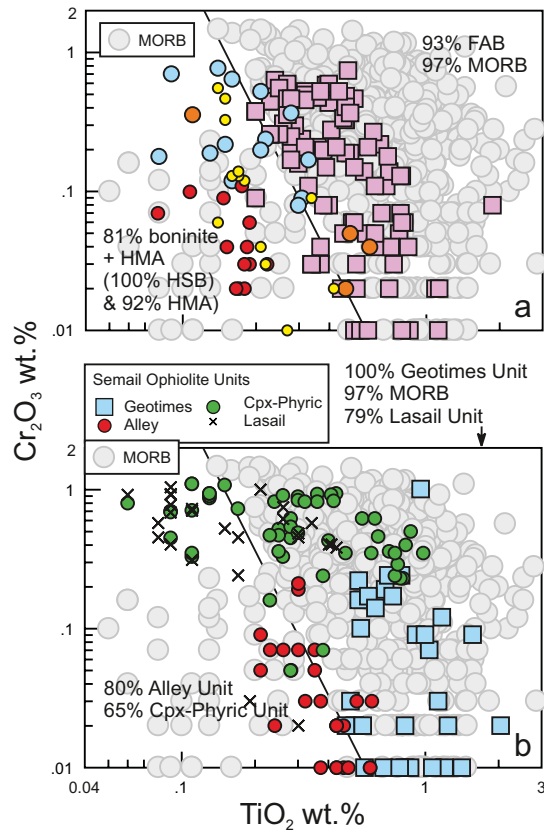
Figure 13 Whattam et al. 2019

Figure 14 Whattam et al. 2020

Figure15 Whattam et al. 2020

Figure 16 Whattam et al. 2020

a Early subduction initiation: 52 Ma
decompressional melting, early seafloor
spreading, construction of FAB crust

$T_C = 1142^o$-1190^oC

DMM

$T_F = 1380^o$-1480^oC

b Continued subduction initiation: 51 Ma
later seafloor spreading, construction of
low-Si boninite crust

$T_c = 1119^o$-1202^oC

$T_F = 1220^o$-1310^oC

increasingly
depleted
DMM

c Latest seafloor spreading: 50 Ma
construction of arc
comprised of high-Si boninite

$T_c = 1125^o$-1190^oC

$T_F = 1220^o$-1310^oC

increasingly
depleted
DMM

decompression
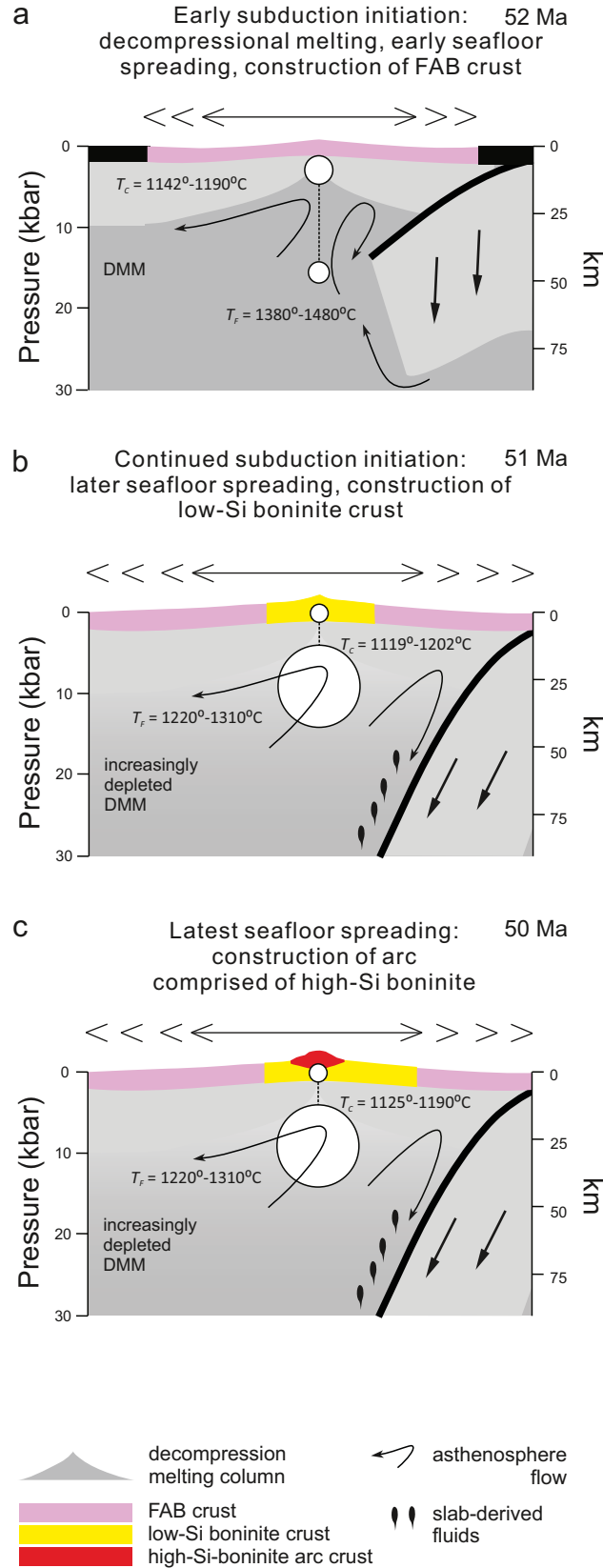melting column

asthenosphere
flow

FAB crust
low-Si boninite crust
high-Si-boninite arc crust

slab-derived
fluids

Figure 17 Whattam et al. 2020